Review

Hyperspectral Imaging for Fresh-Cut Fruit and Vegetable Quality Assessment: Basic Concepts and Applications

Sara Vignati [ID], Alessio Tugnolo *[ID], Valentina Giovenzana [ID], Alessia Pampuri [ID], Andrea Casson [ID], Riccardo Guidetti [ID] and Roberto Beghi [ID]

Department of Agricultural and Environmental Sciences (DiSAA), University of Milan, Via G. Celoria 2, 20133 Milan, Italy; sara.vignati@unimi.it (S.V.); valentina.giovenzana@unimi.it (V.G.); alessia.pampuri@unimi.it (A.P.); andrea.casson@unimi.it (A.C.); riccardo.guidetti@unimi.it (R.G.); roberto.beghi@unimi.it (R.B.)

* Correspondence: alessio.tugnolo@unimi.it

Abstract: During the last two decades, hyperspectral imaging (HSI) has been one of the most studied and applied techniques in the field of nondestructive monitoring systems for the fruit and vegetable supply chain. This review provides HSI technical aspects (i.e., device features) and data analysis approaches (i.e., data processing and qualitative/quantitative modeling) for fresh-cut products, focusing on the different applications which the literature offers and the possible scale-up for process monitoring. Moreover, new frontiers in the development of possible process analytical technologies of cost-effective and hand-held HSI devices are presented and discussed. Even though the performance of these new proximal sensing tools needs to be carefully evaluated, new applicative research perspectives in the development of a proximal sensing approach based on HSI sensor networks are ready to be studied and developed for finding field applications (i.e., precision agriculture, food processing, and more) and enabling faster and more convenient analysis while maintaining the accuracy and capabilities of traditional HSI systems.

1. Introduction

Fresh-cut products are a food preparation conditioned in such a way as to provide a whole series of services to the consumer (including cleaning, hulling, washing, cutting into units or subunits ready to use), while maintaining the characteristics of the freshness and authenticity of the fresh products [1]. However, they are not stable over time due to metabolic processes during the pre- and postharvest stages which cause a variable nutritional value, appearance, and taste [2]. Hence, to ensure consumer satisfaction, food quality, and safety, both the agricultural and food industries have introduced rapid and objective inspection systems throughout the entire product chain.

Human inspection is obviously limited in terms of operator speed and subjectivity and the low amount of product investigated [2], while analytical chemical methods are destructive, time-consuming, labor intensive, often unrepresentative, and environmentally unsustainable [3,4].

Over the last two decades, the development of nondestructive sensing technologies for the automated quality evaluation and safety inspection of agricultural and food products has made substantial progress [3]. Although spectroscopy is considered a powerful tool in this context, it provides a punctual measurement method that is not able to analyze a heterogeneous bulk of samples with sufficient accuracy [3]. For this reason, industries are pointing toward methods that have the process advantages of spectroscopy techniques with the addition of spatial information. This approach, also defined as hyperspectral

imaging (HSI), is nowadays widely applied in the food chain, becoming one of the key elements of process control within the new concept of Industry 4.0.

The increasing number of scientific studies pointing toward a production process control in real-time have pushed to summarize HSI technical aspects and the analysis of the data from such devices to bring the laboratory to the field/production line. The need to have highly customizable tools available at different points in the production process has favored the need to review the literature by focusing on a product category that requires a high degree of quality control, i.e., fresh-cut fruits and vegetables. Therefore, the potential of using this technology along the entire production chain of fresh-cut products emerges, but the limits are also highlighted and represented. Moreover, a discussion on the new frontiers in the development of cost-effective, portable, and hand-held HSI devices, which could open new applicative research perspectives, is presented.

The literature search was performed using the keywords "hyperspectral imaging", "fruit and vegetables", and "quality" and led to the identification of 4509 papers published between 2001 and 2023 (Scopus, 2023). Then, the search was narrowed using the keywords "fresh-cut", and "postharvest", and 104 publications between 2010 and 2023 were identified (Figure 1a—in orange). The same bibliographic search was also performed on the Web of Science platform, obtaining 115 papers published between 2004 and 2023 (Figure 1a—in blue). Both the literature and articles used in this review (Figure 1b) show a general increase in publications over time, particularly in recent years.
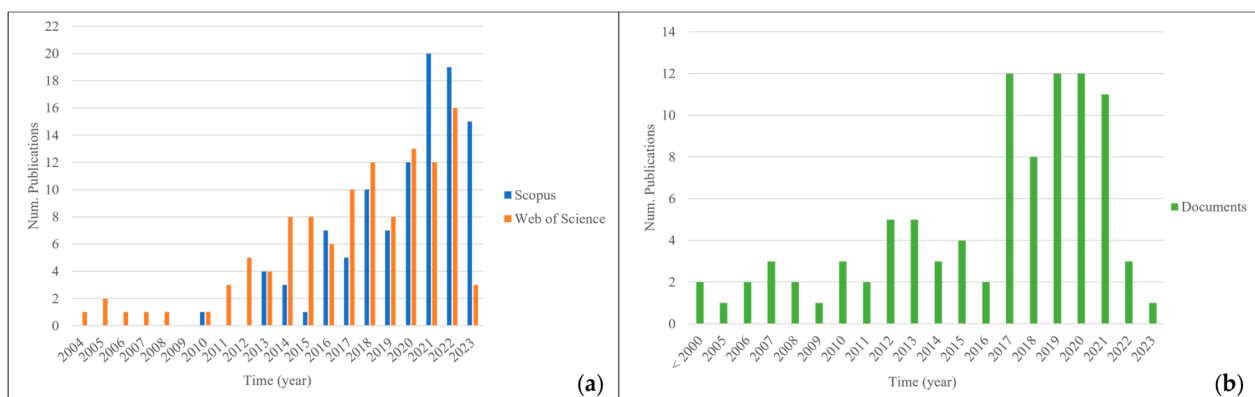

Figure 1. Literature review of the last 20 years using the keywords "hyperspectral imaging", "fruit and vegetables", "quality", "fresh-cut", and "postharvest": documents published and indexed on Scopus and Web of Science (**a**) and documents included in this review (**b**).

2. HSI: Basic Concepts

HSI started to be used in the 80s in remote sensing for agriculture, forestry, geology, environment, ocean, atmosphere, climate change, defense, and security and law enforcement [5,6]. Then, during the 90s, HSI became important also in proximal sensing as a chemical imaging used in food science [7] and postharvest research [8,9] for chemical composition mapping and categorization.

2.1. HSI: Device Components

2.1.1. Light Source

The light source has to be as homogeneous as possible without damaging the sample. The choice of the type of light source (e.g., halogen lamps, light-emitting diodes (LEDs), lasers) depends on the optical range which the latter is able to cover. Halogen lamps operate in ultraviolet (UV), visible (Vis), and infrared (IR) spectral regions, covering a wide spectral range (340–2500 nm) [10]. A filament produces an incandescent emission, which generates a broadband illumination with a smooth continuous spectrum. However, this kind of light source has a few disadvantages, such as a short duration and high heating that can damage

the sample or cause a shift in the spectral peaks, and they can also have an unstable output due to voltage changes and sensitivity to vibrations [4].

LED is a cheap alternative radiation source. This semiconductor light source can produce both narrowband light (at various wavelengths in the ultraviolet, visible, and infrared spectral regions) and high-intensity broadband light. Compared to halogen lamps, LEDs are low-cost components which are compact and durable with low energy consumption, low heat generation, and fast response [4].

While halogen lamps and LEDs are applied in reflectance and transmittance HSI devices, lasers are a directional, narrowband, monochromatic light source widely used in fluorescence and Raman applications, as well as LEDs [2].

2.1.2. Wavelength Dispersion Systems

Wavelength dispersion systems split the incident broadband light or the reflected radiation from the sample into different wavelengths before reaching the detector. Depending on the application, device cost, and sensitivity, different systems like filter wheels, electronically tunable filters (ETFs), and imaging spectrographs (i.e., diffraction grating) can be used.

A filter wheel is a set of discrete bandpass filters mounted on a wheel generally used in multispectral imaging systems (usually able to detect up to 10 wavelengths). They are sensitive to vibration, slow wavelength switching, unchangeable spectral resolution, and image unmatching owing to filter movement. However, they are cost-effective and simple to implement [4].

Concerning ETFs, they disperse the wavelengths one at time (like a bandpass filter) with a moderate spectral resolution (5–20 nm) and broad wavelength range (400–2500 nm). Differently from filter wheels, such filters can be easily customized in an array, reducing mechanical vibration issues [4,10].

Instead, diffraction gratings split instantaneously the broadband light into different wavelengths without moving parts. They are an optical surface composed of a series of closely packed grooves that have been engraved or etched into the grating's surface. Diffraction gratings can be either transmissive or reflective. As light transmits through or reflects off a grating, the grooves cause the light to diffract, dispersing the light into its component wavelengths [4,11].

2.1.3. Detectors

After interacting with the sample, the light carrying the useful information will be acquired by the detector. Detectors convert photons into electrical signals so that the spectral signature can be interpreted. The most common solid-state detectors are charge-coupled devices (CCDs) and the complementary metal-oxide-semiconductor detectors (CMOS). CCD and CMOS sensors comprise many light-sensitive units (photodiodes) whose composition changes (silicon—Si, germanium—Ge, indium gallium arsenide—InGaAs, and mercury cadmium telluride—HgCdTe) according to the spectral range of detection [4,10].

Ge and InGaAs detectors have a suitable energy bandgap for detecting optical signals between 1000 and 1600 nm and 900 and 1700, respectively. Finally, HgCdTe detectors can cover a variety of infrared wavelength ranges, including short/mid- and long-wavelength IR. This versatility makes them suitable for applications ranging from remote sensing to thermal imaging. Silicon detectors are sensitive to UV, visible, and shortwave NIR spectra regions (400–1000 nm), they are cheap, can be miniaturized, and allow high-speed measurements with low noise and a good spectral response. For these reasons, silicon-based CCD cameras have been widely used in hyperspectral imaging systems for the inspection of agricultural products and food quality [4,12].

2.2. Image Sensing and Acquisition Modes

Before reaching the detector, the light radiation interacts with the chemical (activating vibrational effects on molecule functional groups) and physical (light-scattering effects) nature of the sample, and a part can be absorbed (and so turned into heat energy that will never reach the detector), reflected, or transmitted. These interaction processes enable HSI to be implemented in different sensing (Table 1 and Figure 2) and acquisition modes (Figure 3) depending on the sample size and the acquisition time available to perform the analysis, respectively.

Table 1. Imaging sensing mode summary.

| Sensing Mode	Description
Diffuse reflectance (Figure 2a)	The detector and the light source are generally positioned above the sample, and the reflected light from the illuminated area is acquired by the detector. This mode is applied to evaluate external quality properties, such as size, shape, color, surface texture, and physical defects.
Transmittance (Figure 2b)	The sample is placed between the detector and light source, and the radiation which crosses over it is measured. This method is generally used to evaluate internal quality features such as internal defects or chemical compound concentration. However, the sample thickness has an impact on the signal, which decreases as thickness increases.
Interactance (Figure 2c)	The imaging area is isolated from the light source by a predetermined angle or distance. The measured light passes through a little layer of tissue beneath the surface. Thus, it is possible to obtain more information from the inside of the sample than with the reflectance mode.
Fluorescence (Figure 2d)	It measures the radiation emitted by the sample after excitation by absorbing light radiation at a high energy level. The emission is in two main spectral ranges, from blue to green (450–550 nm) and from red to far red (690–740 nm), and it is characterized by three peaks in the blue, red, and far-red bands. In fluorescence imaging, the light source and the detector are positioned at the same side of the sample. Generally, the light excitation sources used are Xenon arc lamps, lasers, or LEDs.
Raman scattering (Figure 2e)	It requires a block of the excitation light from the detection end and an intense excitation light source coupled with a high-performance detector to ensure adequate signal quality. The excitation is typically performed with diode lasers at 785 or 830 nm. As the Raman signals are very weak, commercial Raman imaging systems typically have small imaging areas at the millimeter scales or less (for microscopic applications).
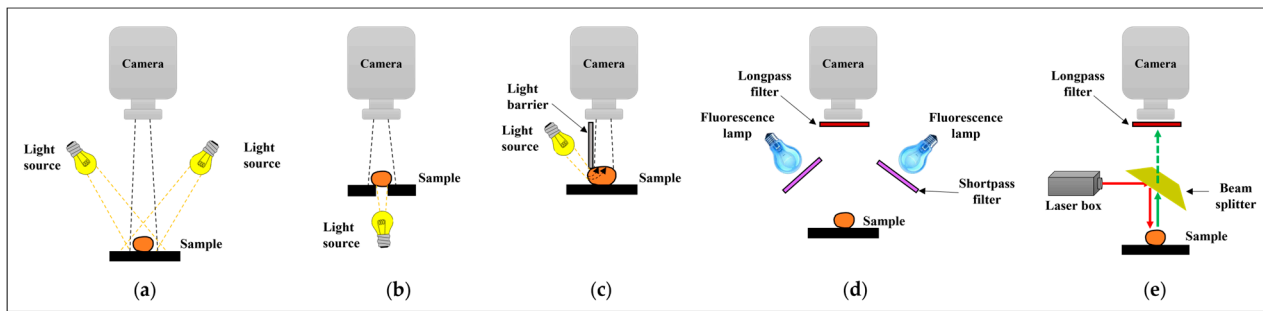
Figure 2. Schematic summary of imaging sensing modes: (**a**) diffuse reflectance; (**b**) transmittance imaging mode; (**c**) interactance imaging mode; (**d**) fluorescence imaging mode; (**e**) Raman scattering mode.
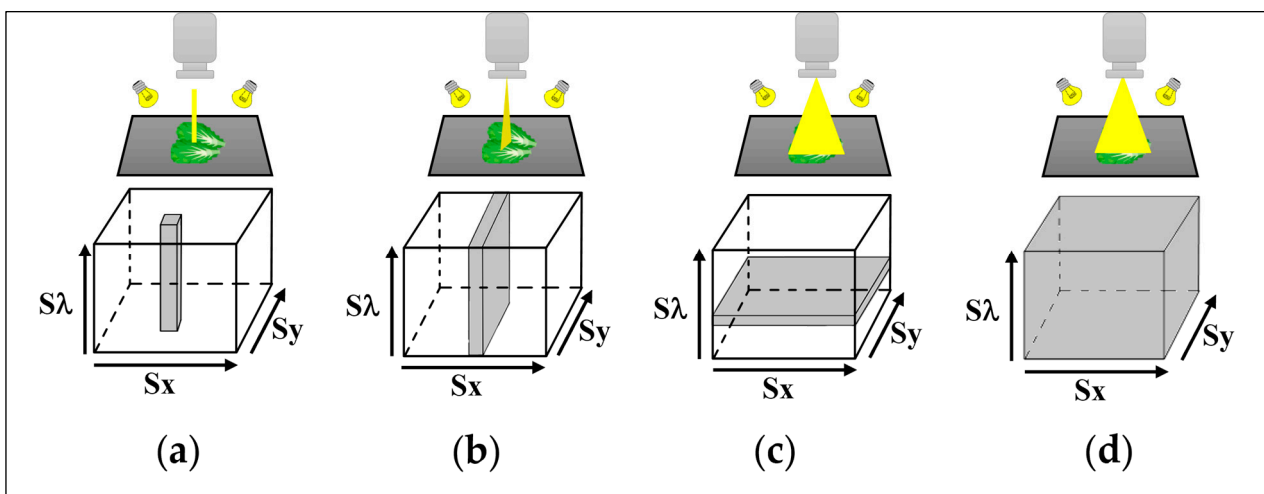

Figure 3. Acquisition modes of a hyperspectral image: (**a**) point scan; (**b**) line scan; (**c**) plan scan; (**d**) snapshot.

3. Software and Image Processing

The hypercube contains the spatial (Sx and Sy) and spectral information (Sλ). The cube composition shows contiguous subimages, one per wavelength (according to the camera resolution) (Figure 4).

Given the three dimensions (Sx, Sy, and Sλ), the hypercube can be handled by unfolding the 3D matrix in a 2D matrix and then refolding after mathematical preprocessing and modeling [13]. Due to the large amount of data (wanted/unwanted information and noise) contained in the hypercube, a statistical approach is needed to explore and analyze the information contained.

For this purpose, different graphical user interfaces (GUIs) are available on programming platforms like MATLAB, Python, or R. Mobaraki and Amigo (2018) proposed an open-source MATLAB-based GUI for hyperspectral image analysis (HYPER-Tools) which integrates fundamental types of spectral and spatial preprocessing methods as well as the main chemometric tools (exploratory data analysis, clustering, regression, and classification) combined with an intuitive process workflow [14]. Thanks to the presence of a powerful visualization provided by MATLAB, such a GUI allows to represent (graphically) a significant amount of information and analyze the results at a glance. An open-source library is available on Python (PyHAT) designed to enable the visualization, thematic image derivation, and spectral analysis of planetary spectral data in a cross-platform [15]. Stand-alone commercial software like ENVI, Unscrambler, and SPSS are also available. ENVI is a powerful remote sensing image processing software that integrates various image processing tools to enhance efficiency. It is preferred for quickly and accurately extracting

information from hyperspectral images and performing spectral analysis. Unscrambler is a software for multivariate data analysis and experimental design, supporting various analyses, data preprocessing, and real-time visualization. SPSS is used for statistical analysis operations, data mining, and the predictive analysis of hyperspectral data [16].
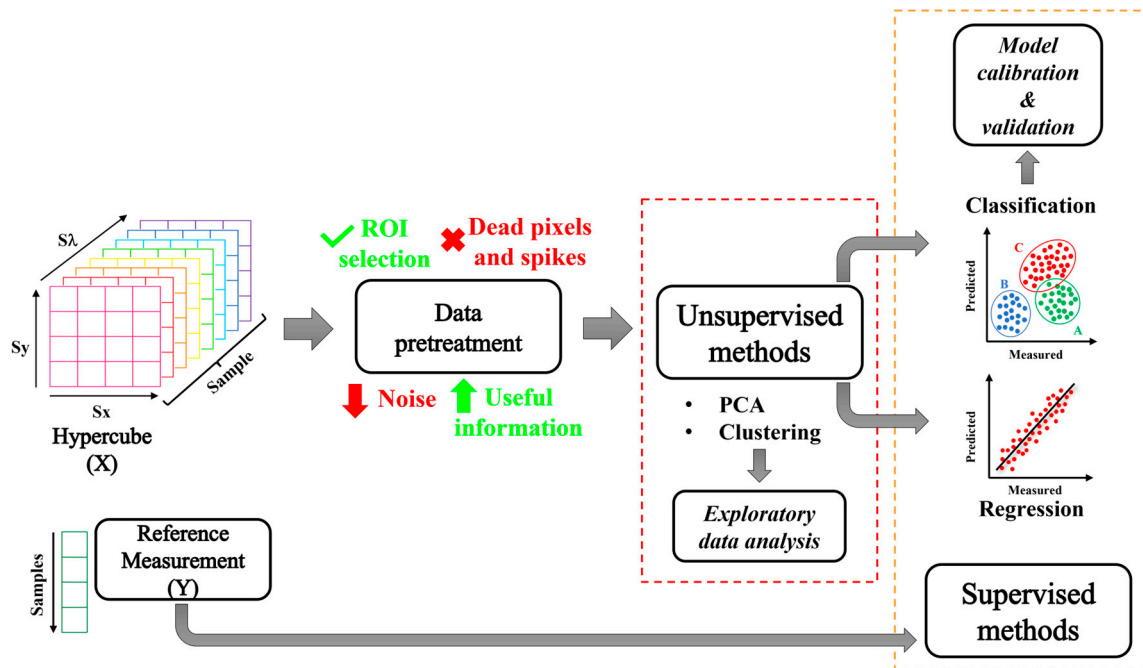

Figure 4. Schematic representation of a hyperspectral image processing analysis.

In order to pick the useful information, the analytical software has to provide the possibility of pretreating the images in order to simultaneously minimize or eliminate unwanted sources of variability (background, redundant information, and artifacts) and maximize information extraction.

Firstly, dead pixels and spectra spikes have to be recognized and harmonized. They are generally due to punctual anomalies of the detector that generate pixels that do not record the correct information. Dead pixels are present as missing or zero values, and they can be present singly, in full lines, at specific wavelengths, or throughout the entire spectrum signal. Detecting missing scan lines and dead pixels can be achieved using different algorithms with major or minor complexity (like thresholding techniques, genetic or evolutionary algorithms, or a minimum volume ellipsoid (MVE)). Instead, spikes are unexpected and with high intensity peaks of the signal, and they are usually substituted with the mean or median of a spectral window with the spike point at its center. Once the missing scan lines, dead pixels, and spikes have been detected, one straightforward manner to replace them is using the mean or median of the spectral of the neighboring pixels [17].

Then, the regions of interest (ROI) have to be identified. If the sample does not cover the entire scanned area, the scanned area has to be isolated from the background and the presence of shadows caused by the sample and light source position. Several techniques like (i) manual selection, (ii) predeterminate single wavelength, (iii) principal component analysis (PCA) and (iv) cluster analysis can be used in order to create a "mask" capable of isolating the ROI [14] as reported in Figure 5.
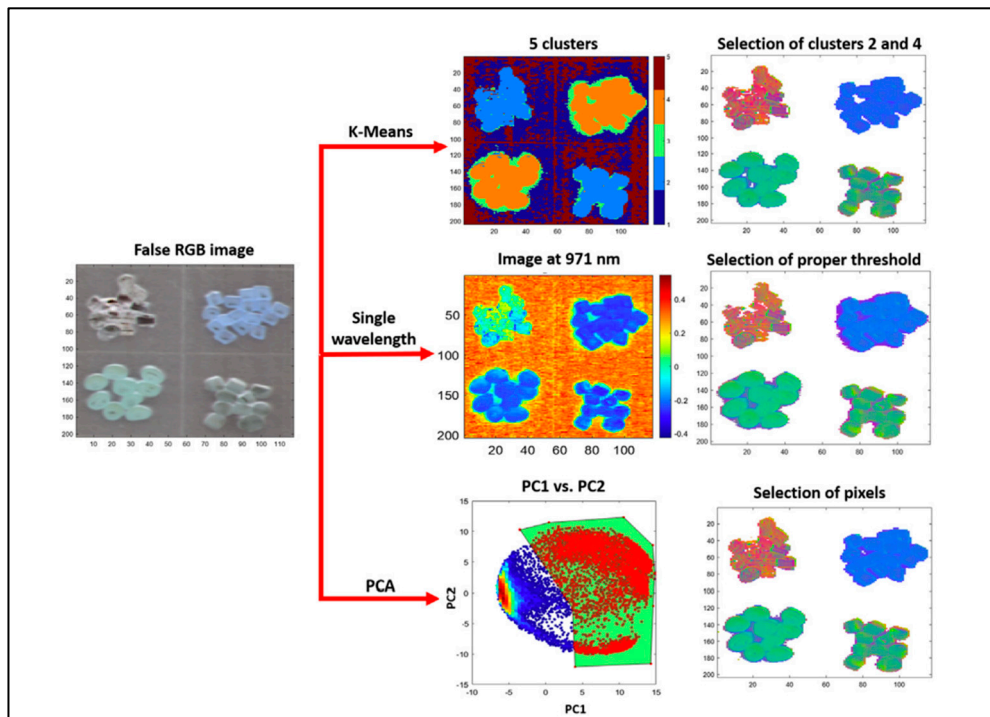
Figure 5. Depiction of three different methodologies (k−means analysis, wavelength selection, principal component analysis) for background. Reprinted with permission from Ref. [17]. 2019, Elsevier.

Finally, spectra may need to be preprocessed to reduce the noise associated with the data, minimize artifacts, and amplify the information. In principle, well-known spectral preprocessing methods applied to spectroscopy are also used in hyperspectral imaging. However, preprocessing techniques must be handled with care, taking into account the possible loss of some information, resulting in a decrease in spatial and/or spectral resolution, and the final goal of the analysis. Figure 6 graphically summarizes the most common mathematical pretreatments performed on NIR spectra labeled according to the percentage of moisture content (MC %) of the samples (Figure 6a shows the raw spectra). Many smoothing methods (e.g., Gaussian filter, moving average, median filter, and Savitzky–Golay (SG) smoothing) are used as a filter to reduce spectral noise. Additive and multiplicative effects are very common in optical data, influencing the global intensity (typically arising from unwanted light scattering) and/or producing baseline vertical shifts (offsets). For these reasons, treatments like standard normal variate (SNV, Figure 6b) transform or the multiplicative scatter correction (MSC Figure 6c) are generally applied. Derivation methods (usually first and second derivative, Figure 6d) are also used to enhance the resolution and minimize the spectra offset and drifts. Finally, different column-wise normalization and/or scaling treatments (like mean centering, autoscaling, range scaling, Pareto scaling, etc.) become fundamentals to homogenize the data to perform a correct explorative and modeling phase (Figure 6e). Since the variance values depend on the scale of the variables, it becomes difficult to compare and impossible to combine information from variables of different nature, unless properly normalized [18–20]. Moreover, different combinations of these methods applied simultaneously can also be used for signal processing [21].
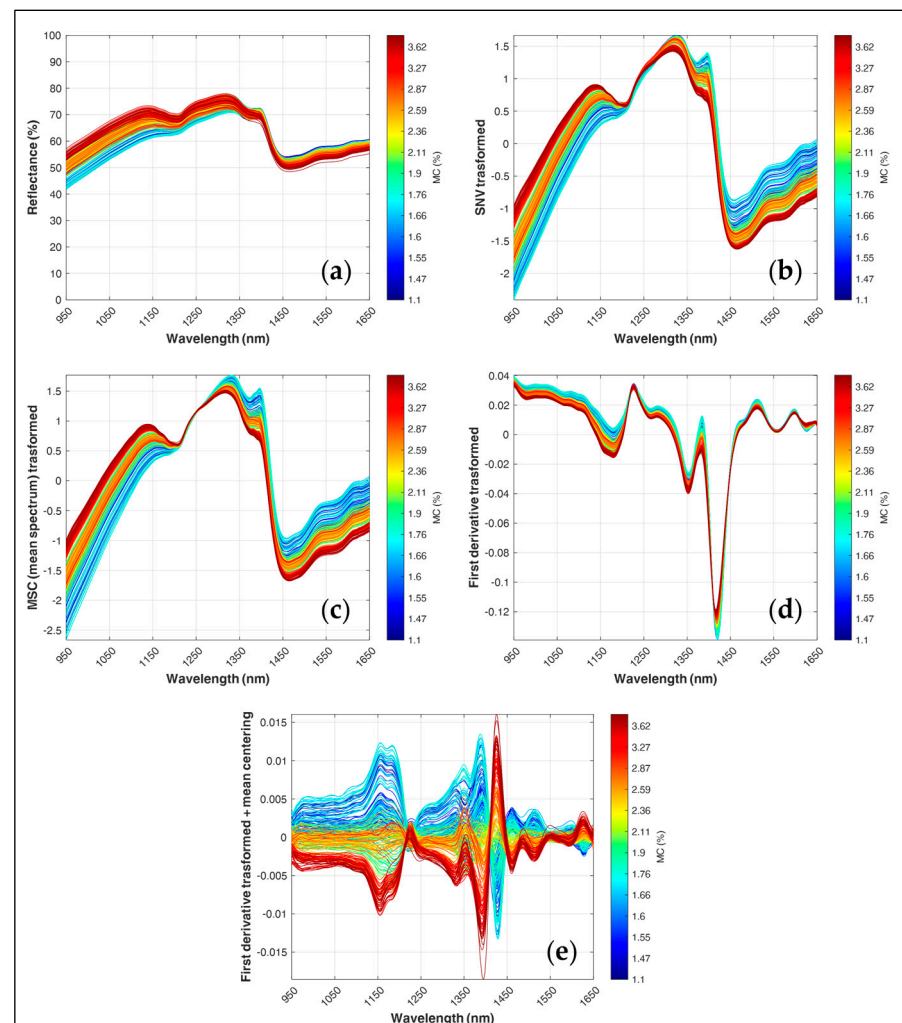
Figure 6. Spectra of samples labeled according to the percentage of moisture content (MC%): (**a**) Raw spectra, (**b**) SNV transformed spectra, (**c**) MSC transformed spectra, (**d**) Savitzky−Golay first derivative transformed spectra, (**e**) Savitzky−Golay first derivative transformed normalized with mean centering.

3.1. Multivariate Statistical Analyses

After image preprocessing, multivariate statistical analysis is needed to extract useful information and easily show the relationship between hyperspectral data and the feature of the sample under evaluation. Multivariate analyses can be divided into two main groups: unsupervised and supervised methods.

3.1.1. Unsupervised Methods

Unsupervised methods give qualitative information of the analyzed data. Without any prior assumption, they allow to (i) group samples sharing similar features, (ii) identify outliers or anomalous data trends, and (iii) identify correlations among variables and interactions between samples and variables. Principal component analysis (PCA) is one of the most common unsupervised methods applied to HSI to extract useful information. PCA seeks a linear combination of the original variables (wavelength) to produce new variables (the principal components, PCs) orthogonal to each other which account for the variance of the original ones in a new space of projection. Furthermore, it describes the sample distribution highlighting trends and groups, it permits to understand any variable correlation, and to sort and select variables according to relative importance [13]. Instead, other methods find potential clusters in the data in a nonhierarchical or hierarchical

manner [22]. The former includes k-means clustering that divides the observations into a predetermined number of groups (*k* clusters), and a sample is placed in a cluster with the nearest barycenter. On the contrary, hierarchical techniques create a hierarchy of clusters using the distance between pairs of samples, and it is typically displayed as a dendrogram [4].

3.1.2. Supervised Methods

Supervised classification and regression techniques (Table 2) can be used according to the specific application to predict qualitative or quantitative features by finding a relationship between a set of independent variables (optical outputs) that describes the objects (predictors) studied and a set of measured responses for the same objects [23,24].

Multivariate classification methods define the existing relation between the experimental variables (X matrix, the hypercube) and a qualitative variable that identifies the belonging class (y vector, response variable). Many methods like linear discriminant analysis (LDA), k-nearest neighbor (KNN), soft independent modeling of class analogy (SIMCA), support vector machine (SVM), and partial least square regression–discriminant analysis (PLS-DA) are used to define the membership of each sample to its appropriate class [25].

Multivariate regression methods calculate the mathematical model for the relation between the X matrix and the y vector of the quantitative response [26]. The regression model design using HSI data is different from developing a traditional spectroscopic model, where each spectrum (X_i) has a corresponding measured variable (y_i). Indeed, in hyperspectral images, there can be found thousands of spectra for the same measured variable, and a spectrum that represents the sample is calculated. The mean spectra for each sample are combined to create the data set (X), which is used with regression techniques to predict the corresponding observed values (y) [27]. For these purposes, methods like multiple linear regression (MLR), principal component regression (PCR), partial least square regression (PLSR), support vector machine regression (SVR), or artificial neural networks (ANNs) are broadly used [28].

Table 2. Overview of the classification and regression algorithms used for fresh-cut fruit and vegetable analysis.

Method [1]		Reference
Classification	PLS-DA	Diezma et al. [29], Everard et al. [30], Rady et al. [31], Pu et al. [32], Zhu et al. [33], Babellahi et al. [34]
	LDA	Lee et al. [35], Delwiche et al. [36]
	KNN	Rady et al. [31], Pu et al. [32],
	SIMCA	Pu et al. [32], Ríos-Reina et al. [37]
	SVM	Cen et al. [38], Zhu et al. [33], Bai et al. [39]
Regression	PCR	van Roy et al. [40], Xu et al. [41]
	PLSR	Rady et al. [31], van Roy et al. [40], Yan et al. [42], Amodio et al. [43], Mo et al. [44], Zhu et al. [45], Rahman et al. [46], Ramos-Infante et al. [47], Chaudhry et al. [48], Xiao et al. [49], Babellahi et al. [34], Shrestha et al. [50], Eshkabilov et al. [51], Wang et al. [52], Li et al. [53], Lan et al. [54], Xu et al. [41]
	MLR	Lu and Peng [55], Peng and Lu [56], Rajkumar et al. [57], Zhu et al. [45]
	ANNs	Siripatrawan et al. [58], Li et al. [53]
	SVR	Zhang et al. [59], Chen et al. [60], Pang et al. [61]
	LS-SVM	Zhu et al. [45], Xiao et al. [49]

[1] PLS-DA = partial least square–discriminant analysis; LDA = linear discriminant analysis; KNN = k-nearest neighbor; SIMCA = soft independent modeling of class analogy; SVM = support vector machine; PCR= principal component regression; PLSR = partial least square regression; MLR = multiple linear regression; ANNs = artificial neural networks; SVR = support vector regression; LS-SVM = least square support vector machine.

4. HSI in Fresh-Cut Product Quality Assessment

Fresh-cut products are generally characterized by high quality levels, but they deteriorate faster than intact items as a result of damage caused by minimum processing, which speeds up various physiological changes that lead to a decrease in product quality and shelf life. Discoloration-increased oxidative browning at cut surfaces, flaccidity due to water loss, and lower nutritional value are all signs of produce deterioration. Moreover, the damaged tissues are a good growing medium for some pathogenic microorganisms and harmful to human health [62] (Table 3). So, the quality assessment of fresh-cut foods is one of the most important goals of the highly competitive food industry [63] and, in recent years, the evaluation of these characteristics is one of the principal applications of HSI [64].

Table 3. Description of quality features for fresh-cut products.

	Qualitative Features		Description
External features	Color		First element of quality monitoring and conveys consumer choice. It is an indirect indicator of features like freshness, desirability and variety, maturity, and safety, which are related to the physical, chemical, or microbial changes that occur in ripeness and the postharvest processing and handling stages [65].
	Defects	Surface defects	Mainly due to mechanical injuries, insects, diseases, and over- or under-ripeness. Damaged products should be selected and removed, during postharvest processing, to reduce losses by avoiding secondary contaminations [66].
		Physiological disorders	Appear during postharvest after internal or external stresses, like nutritional deficiency, senescence, suppressed respiration, and extreme temperature [2].
		Chilling injury	Caused mainly by postharvest storing at low temperatures which produces internal browning, deteriorated texture, juiciness deficiency, and unpleasantness [64].
Internal features	Texture		Capacity to withstand deformation actions like biting, chewing, and grinding, with an impact on food acceptability and consumer preferences [64]. Firmness is an indicator of the maturity stage and shelf life. Firmness loss in fruits is primarily caused by the enzymatic degradation of pectin present in the intercellular space and cell wall [62].
	Nutritional value		Represented by the caloric intake or elements that are important from a nutritional point of view.
Safety	Absence of antinutritional substances		e.g., nitrates and nitrites, pesticide residues, insect or pest infestation, fecal contamination, naturally occurring undesirable compounds, and plant growth regulators [2,67].
	Absence of pathogenic microorganisms		e.g., *Escherichia coli*, *Salmonella* spp., and *Listeria monocytogenes* whose presence is caused by soil or manure contamination, irrigation water, inappropriate packaging, and inadequate storage temperatures [68].

Table 4 summarizes (according to each product category) the main HSI applications of the last decade to identify and evaluate the critical quality parameters of fresh-cut products. In general, while various products have been examined, the literature demonstrates plenty of applications using HSI devices that retrieve qualitative optical data (within 400–1000 nm) useful to develop qualitative and/or quantitative predictive models with significative applicative performance. In this context, another essential factor is the possibility of transfer calibration models among different devices. On this topic, punctual spectroscopy finds a well described literature, while much less research is available on the calibration transferability between HSI devices which may have different imaging and/or lighting configurations. Hence, forthcoming research is needed focusing on enhancing data mining and calibration transfer techniques to fully harness the future needs and perspectives described in Section 5.

4.1. Fresh-Cut Green Leafy Vegetables

4.1.1. Lettuce

Mo et al. (2015) applied a Vis-NIR (400–1000 nm) HSI device in reflectance to discriminate sound and discolored lettuce areas on both abaxial and adaxial surfaces. A one-way ANOVA was used to determine the optimal wavelengths for discrimination purposes. Two indexes were developed (waveband ratio imaging, RI, and subtraction imaging, SI) to improve classification accuracy. In particular, the best classification performances (prediction accuracy, sensitivity, and specificity > 99.9%) were achieved by RI between 552 and 701 nm ($RI_{552/701}$) and SI for 557–701 nm ($SI_{557-701}$) [69].

Again, Mo et al. (2017) proposed an on-line detecting system based on reflectance HSI (Figure 7) (400–1000 nm) to discriminate contaminants (i.e., slugs and worms) from sound lettuce. SI was used to classify slugs, resulting in a classification accuracy of 97.5%, sensitivity of 98.0%, and specificity of 97.0%, while RI was used to discriminate worms, achieving classification accuracy, sensitivity, and specificity rates of 99.5%, 100.0%, and 99.0%, respectively [70].
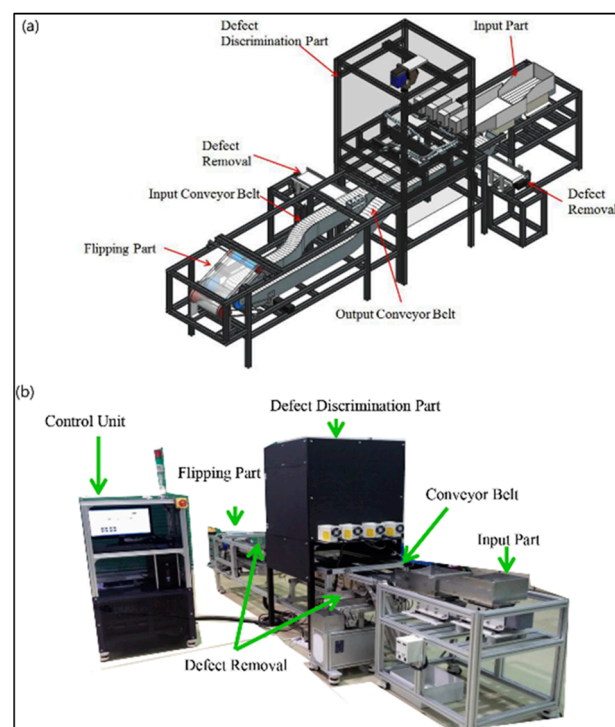

Figure 7. Schematic representation (**a**) and picture (**b**) of the on-line detecting system developed by Mo et al. (2017). Reprinted with permission from Ref. [70]. 2017, Elsevier.

Fresh-cut lettuce can be sold in modified atmosphere packaging (MAP), but the tissue decay can begin a few days later after processing. Simko et al. (2015) proposed two lettuce decay indexes (LEDIs) to identify both tissues damaged by cold temperatures and lettuce deterioration ($LEDI_{CF}$, based on the maximum and minimum level of chlorophyll fluorescence, and $LEDI_4$, based on reflectance imaging using 677, 744, and 904 nm), achieving about a 97% accuracy in categorizing tissue as being fresh or decayed without removing the MAP [71].

Instead, Eshkabilov et al. (2021) applied reflectance HSI (400–1000 nm) and developed a multivariety model to quantify micro- and macronutrients (i.e., nitrate, calcium, potassium, and soluble solid content (SSC)), pH, and chlorophyll concentration. Two bands were selected as the most informative, 506–601 nm and 634–701 nm, and used to build PLS models with a good prediction capability for all parameters (R^2_p = 0.78–0.99) [51].

Concerning safety assessment, Cho et al. (2018) applied fluorescence HSI on romaine lettuce leaves to detect four animal (dairy cattle, pigs, chickens, and sheep) fecal species contaminations. For discriminating feces from the four animal species, single fluorescence wavebands were found, F641 nm, F505 nm, F633 nm, and F645 nm, respectively, for dairy cattle, pig, chicken, and sheep feces, and the ratio between F692 and F668 was used to identify any fecal trace with an accuracy from 80% to 100% according to the fecal dilution level [72].

4.1.2. Spinach Leaves

Zhu et al. (2019) investigated the adequacy of hyperspectral imaging for the evaluation of the freshness of spinach leaves during storage at different temperatures. They applied visible-SWNIR (380–1030 nm) and NIR reflectance (874–1734 nm) HSI systems. After data preprocessing and wavelength selection, the following models were applied and evaluated: PLS-DA, SVM, and ELM (extreme learning machine). All three models achieved good results, with above 92% accuracies for both spectra. Although good results were achieved, the data processing techniques were time-consuming, which is a barrier to practical deployment. Moreover, to improve the models' robustness, the sample size should be increased, and new types of samples should be used in future investigations [33].

Siripatrawan et al. (2011) proposed an HSI device (400–1000 nm) to measure the contamination degree of *Escherichia coli* in packaged fresh spinach. PCA was applied for wavelength selection, and ANNs were used to predict the number of colonies of *E. coli* ($R^2_p = 0.97$) and obtain a prediction map of the microorganism number to pixel spatial information, allowing a rapid and useful data interpretation [58].

Instead, Everard et al. (2014) used both reflectance (Vis-NIR) and fluorescence (UV and violet) HSI devices to detect fecal contamination (in different concentrations) on spinach leaves. PLS-DA and two indexes based on wavelength ratio were used to compare the two HSI devices (Figure 8). The results showed that UV and violet fluorescence had better performances (from 87% to 100% accuracy depending on the degree of dilution) than the Vis/NIR reflectance device, where the accuracy decreased sharply with increasing dilution [30].
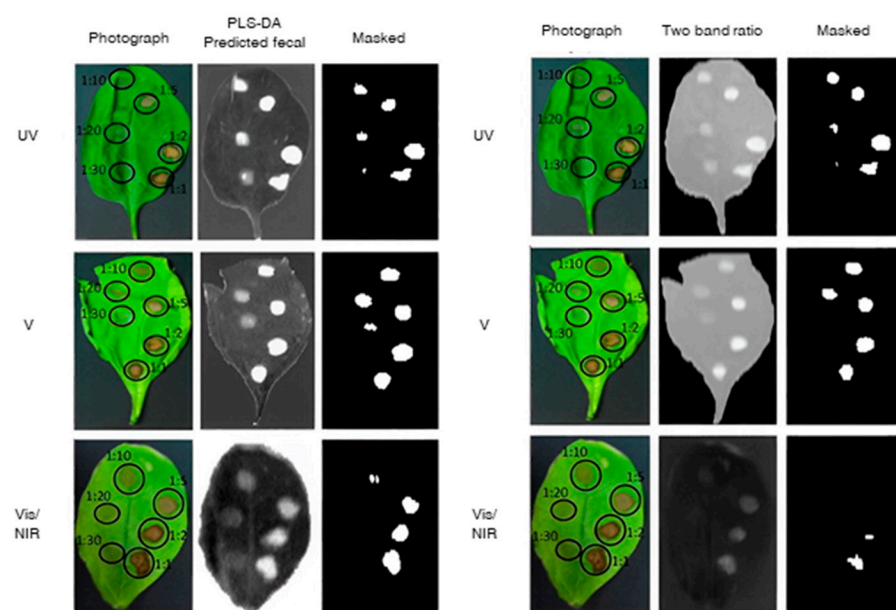

Figure 8. Examples of fecal contamination detection on *Spinacia oleracea* leaves for each HSI image configuration (UV at 370 nm, violet "V" at 410 nm, Vis/NIR) paired with PLS-DA (on the (**left**)) and wavelength ratio (on the (**right**)) analyses. Adapted with permission from Ref. [30]. 2014, Elsevier.

4.1.3. Rocket

Generally, rocket has a shelf life of 7 to 14 days, depending on the combination of different factors (i.e., raw material conditions, manipulation, processing and storage temperature). In 2018 and 2020, Chaudhry et al. proposed a multivariate approach based on PCA and PLS scores for a shelf-life estimation (multivariate accelerated shelf-life testing) and concentration mapping of the vitamin C (Figure 9), ascorbic acid, and phenols of stored rocket leaves. Vis/NIR and NIR his devices were used to reach these goals, showing the capability to use spectra as a quality attribute to simulate a degradation kinetic using the PCA principal components and quantify vitamin C (R^2 = 0.76 and RMSEP = 10.90 mg/100 g), ascorbic acid (R^2 = 0.73 and RMSEP = 10.24 mg/100 g), and phenols (R^2 = 0.78 and RMSEP = 13.81 mg gallic acid/100 g) [48,73].
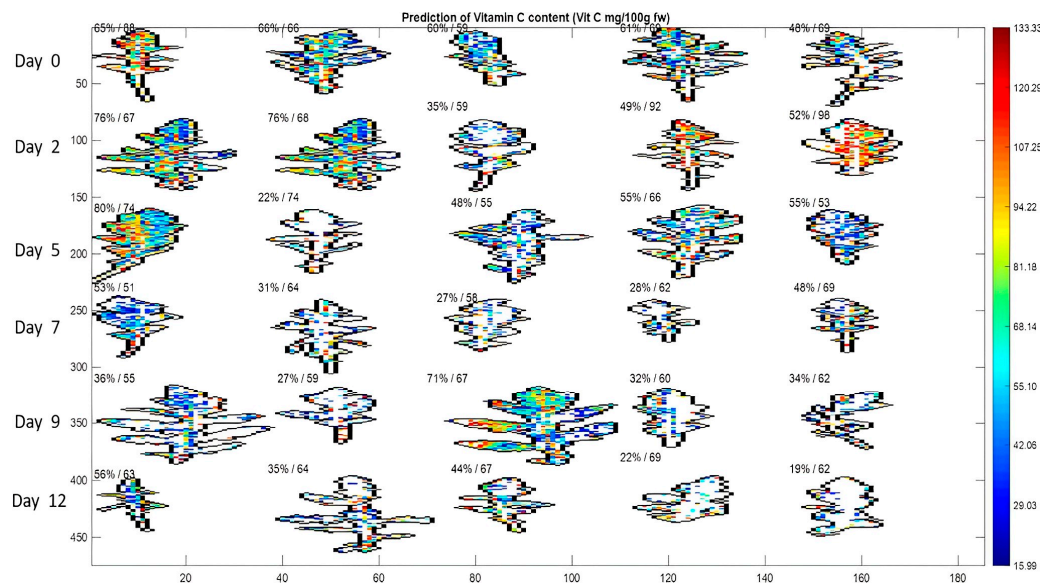

Figure 9. PLS vitamin C prediction map from day 0 to day 12 proposed by Chaudhry et al. (2020). For each leaf is indicated the percentage of pixels predicted within the calibration range and the average vitamin C concentration over these pixels. Reprinted with permission from Ref. [48]. 2020, Elsevier.

4.2. Fresh-Cut Tubers

Potatoes

Color, water, and starch content are quality indicators of fresh-cut potatoes [49,52]. Also, in this case, Vis/NIR HSI systems were demonstrated to be effective tools to build prediction maps (Figure 10) for the distribution of such qualitative indicators using different modeling approaches (PLS, SVM, and LS-SVM). Indeed, for color and water content prediction, an R^2 about 0.8 was obtained using any of the modeling methods [49], while Wang et al. (2021) extracted a bulk of characteristic wavelengths (about 10 to 30 wavelengths according to the applied selection method) to build a PLS model for the starch content prediction (R^2 = 0.95 and RMSEP of 1.63 g kg^{-1}) [52].

However, one of the major problems related to fresh-cut potatoes is the foodborne contamination of *Escherichia coli* [53]. Tao et al. (2019) proposed a curcumin-based photodynamic treatment to deactivate the *E. coli* proliferation on the surface of stored fresh-cut products [74]. In this case, HSI was used by Li et al. 2021 to explore the illumination time of the photodynamic treatment with the best inactivation effect. A back-propagation neural network approach was used to develop quantitative predictive models for colony quantification using both full spectrum and selected wavelengths (R^2 = 0.97, 0.88; RMSEP = 0.065 log CFU g^{-1}, 0.142 log CFU g^{-1}, respectively), identifying 20 min as the optimum treatment time [53].
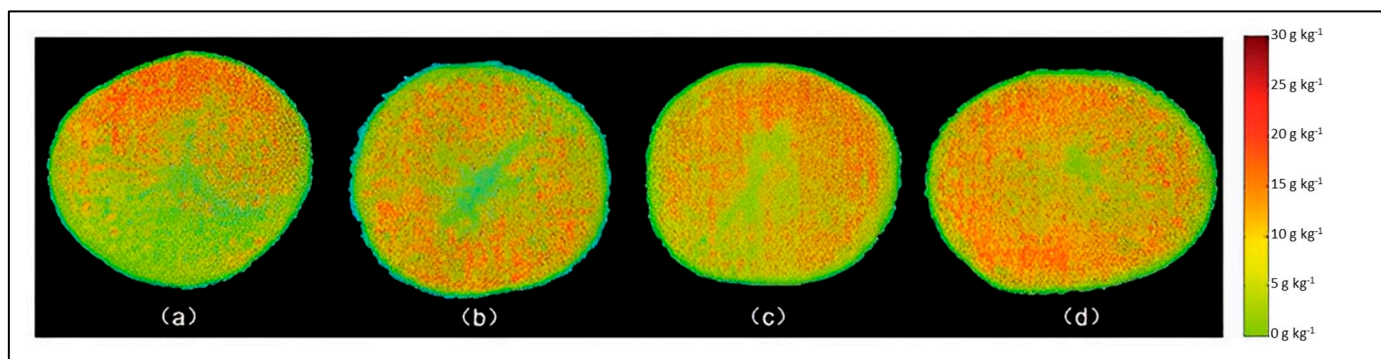
Figure 10. Fresh-cut potato starch distribution maps of the content in (**a**) 11.8 g kg^{-1}; (**b**) 13.5 g kg^{-1}; (**c**) 19.0 g kg^{-1}; and (**d**) 21.6 g kg^{-1} (Wang et al., 2021). Reproduced from Ref. [52] with permission from The Royal Society of Chemistry.

4.3. Fresh-Cut Fruits

4.3.1. Tomato

Tomatoes are one of the major fresh-cut vegetables consumed, and the detection of cracking defects is very important to avoid any development of pathogenic microbes that may have harmful consequences on consumer health. Thus, Lee et al. (2011) applied HSI (1000–1700 nm) to detect damaged tomatoes. The authors applied PCA on the full spectrum and four selected wavelengths (1078 nm, 1194 nm, 1425 nm, and 1642 nm) to extract and compare PC images for crack detection. Finally, LDA was applied for improving the discriminant ability between sound and cracked tomatoes, showing a classification accuracy of 91.7% (using full NIR spectrum) and 80.6% (using only four wavelengths) [35].

4.3.2. Cucumber

Cen et al. (2016) applied reflectance (500–675 nm) and transmittance (675–1000 nm) hyperspectral imaging to detect chilling injuries, using an on-line HSI system developed by Ariana and Lu (2008) and Lu and Ariana (2013) [75,76]. Supervised classification models were developed using selected wavelengths (obtained using different wavelength selection methods) to classify in two (i.e., safe and damaged) and three classes (i.e., safe, lightly damaged, and severely damaged) based on the spectral and image analysis at specific two-band ratios. SVM resulted as the best classifier method, allowing to achieve a total classification accuracy of 100% for the two-class classification, and an overall accuracy of 90.5% for the three-class classification [38].

4.3.3. Green Bell Pepper

Storage chilling injuries were evaluated also on green bell peppers by Babellahi et al. (2020) with HSI (400−2500 nm). A PLS-DA model was developed to distinguish cold-stored fruit (4 °C) from fresh fruit and fruit stored at higher temperatures (12 °C) using selected Vis-NIR (694, 719, 751, 813, 886, and 973 nm) or NIR variables (1138, 1244, 1379, and 1642 nm). The model in the Vis-NIR achieved an 83% NER (nonerror rate) in cross-validation, while the model with NIR wavelengths reached a cross-validation NER equal to 81%. Moreover, a PLSR model was developed to predict days of storage at 4 °C, in order to take any corrective action to avoid further damage. The model was built based on the data extracted from Vis-NIR HSI and using selected wavelengths from VIP (variable importance in projection) scores. Good predictive performances were obtained (R^2_{CV} = 0.79, and RMSE$_{CV}$ = 0.5 days of storage at 4 °C), demonstrating that it is a good option for the early detection of CI of green bell peppers and also for industrial on-line applications [34].

4.3.4. Apple

Fresh-cut apple processing can lead to browning reactions that strongly influence the purchase of the end consumer. Browning is the consequence of a series of biochemical

reactions under the polyphenol-oxidase enzyme's activity. In this case, HSI can be used to detect these damages beforehand [77]. The development of brown pigments is common in fresh-cut and dried apple slices. Shrestha et al. (2020) demonstrated that polyphenol-oxidase activity was mainly detectable around 677 nm, proposing a robust detection algorithm independent from cultivars and treatments [50].

Moreover, nutritional features are another important indicator of acceptability, especially in fresh-cut apples. NIR-HSI (1000–2500 nm) was applied by Lan et al. (2021) to evaluate the contents of dry matter, total sugar content, fructose, glucose, sucrose, malic acid, and polyphenols. NIR-HSI images were acquired on the surface of apple slices, and PLS models were developed and successfully used to describe the dry matter ($R^2_{CV} = 0.83$, RMSE = 9.7 g kg^{-1}) and total sugar content ($R^2 = 0.81$, RMSE = 8.4 g kg^{-1}) distribution, as shown in Figure 11 [54].
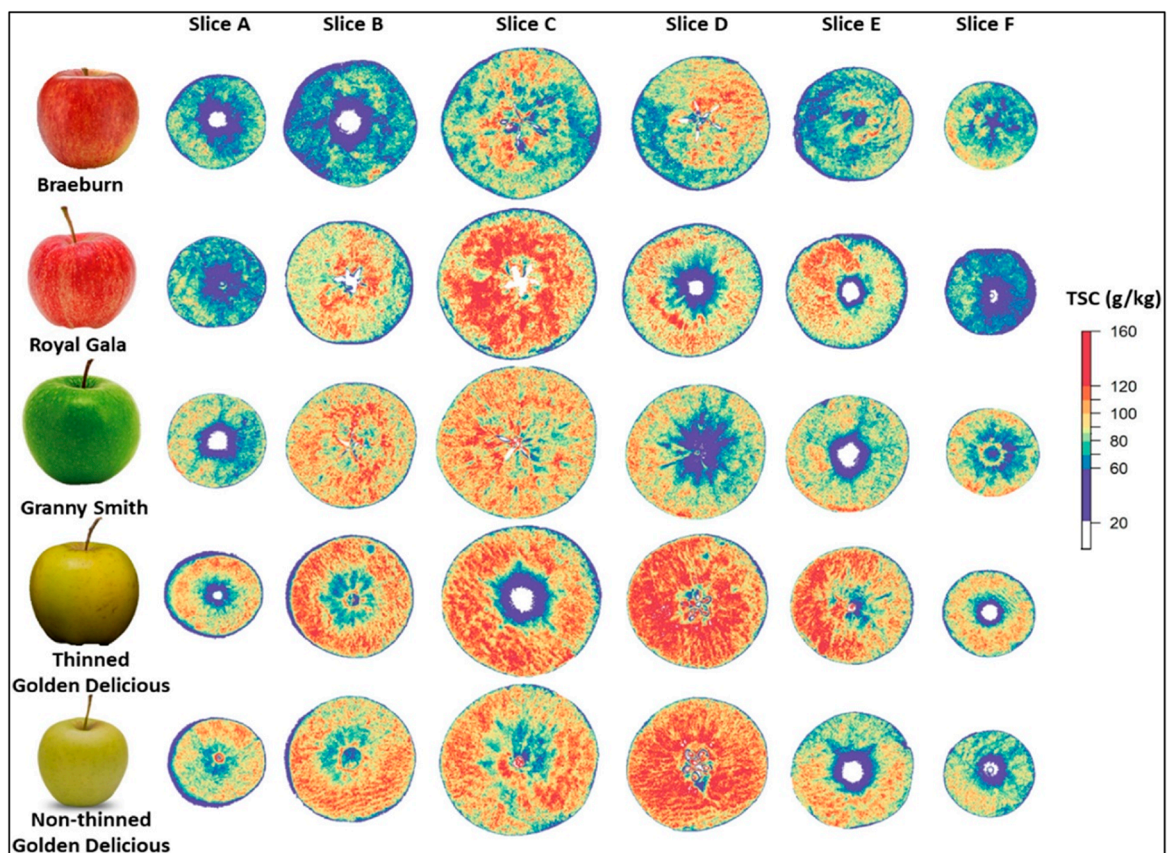

Figure 11. Distribution of total sugar content (TSC) in apple slices predicted by the PLS models proposed by Lan et al. (2021). Reprinted with permission from Ref. [54]. 2021, Elsevier.

4.4. Fresh-Cut Vegetables

4.4.1. Celery

Fresh-cut celeries, one of the most widely consumed vegetables, are very rich in fibers. Yan et al. (2017) applied an HSI device (380–1000 nm) to quantify the soluble and insoluble dietary fiber in celery, and their spatial distribution was visualized at 0, 7, 14, 21, and 28 days of storage (Figure 12). Celeries showed interesting spectral variability values in the shortwave near-infrared region (from 780 to 1008 nm). Different PLS prediction models were developed using a variant of the PLS method (the genetic synergy interval partial least square, GA-Si-PLS) to select the optimal wavelengths with minimal redundant information. The obtained models showed high prediction performance for both (R^2 equal to 0.96 and 0.97 and RMSE of 1.18 g/100 g and 0.34 g/100 g, respectively) insoluble and soluble fiber [42].
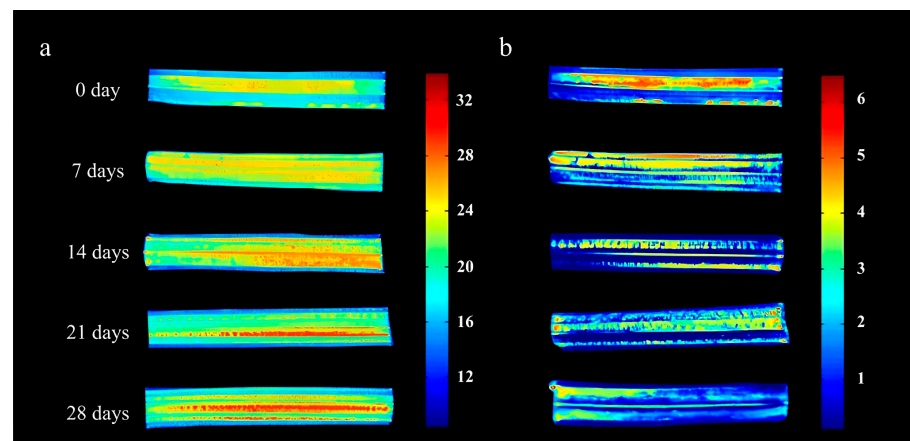
Figure 12. Insoluble (**a**) and soluble (**b**) fiber distribution map of fresh-cut celeries during the storage periods of 0 day, 7 days, 14 days, 21 days, and 28 days, respectively. Reprinted with permission from Ref. [42]. 2017, Elsevier.

4.4.2. Cabbage, Carrot, Green Onion, Onion, Potato, Radish, and Zucchini

Fresh-cut vegetables can contain foreign materials (FMs) such as small plastic pieces or biological contaminants (i.e., bugs, worms), and helpful methods of detecting FMs in industrial processing operations are required. Therefore, Tunny at al. (2023) evaluated the performances of three HSI techniques (Vis/NIR, SWIR, and fluorescence) combined with a PLS-DA model to identify different types of FMs in various fresh-cut vegetables. The results showed a good performance with an accuracy of 99% with SWIR, followed by Vis/NIR (89%), and fluorescence (64%). Moreover, from the SWIR data were selected ten wavelengths (912, 935, 965, 1082, 1188, 1288, 1417, 1576, 1770, and 1858 nm), and the obtained accuracy of the new PLS-DA model was similar to that of the original one (99%), suggesting the suitability of this HSI technique to be applied in an industrial context [78].

Table 4. Hyperspectral imaging applications in fresh-cut quality.

Fresh-Cut Product	Quality Features	Spectral Range	Sensing Mode	Modeling Method	Performances	Reference
Lettuce	Color	400–1000 nm	Reflectance	Classification SI and RI	Accuracy, sensitivity, and specificity > 99.9%	Mo et al. [69]
	Color–Browning	400–1000 nm	Reflectance	ANOVA, Classification SI and RI	Accuracy = 97.0–100.0%	Mo et al. [79]
	Decay	380–1012 nm	Reflectance and Chlorophyll Fluorescence	Classification	Accuracy = 97.0%	Simko et al. [71]
	Relative water content, chlorophyll, and carotenoid	400–1000 nm	Reflectance	Wavelength ratio	–	Shurygin et al. [80]
	Nutrient levels: NO_3^-, Ca^{2+}, K^+, SSC, pH, SPAD	400–1000 nm	Reflectance	PLSR, PCA	R^2 = 0.78–0.99	Eshkabilov et al. [51]
	Fecal contamination	400–800 nm	Fluorescence	Classification RI	Accuracy = 80.0–100.0%	Cho et al. [72]

Table 4. *Cont.*

Fresh-Cut Product	Quality Features	Spectral Range	Sensing Mode	Modeling Method	Performances	Reference
	Foreign substances (slugs and worms)	400–1000 nm	Reflectance	Classification SI and RI	Accuracy = 97.5%, sensitivity = 98.0%, and specificity = 97.0% with SI Accuracy = 99.5%, sensitivity = 100.0%, and specificity = 99.0% with RI	Mo et al. [70]
	Foreign substances (worms)	400–1000 nm, 980–1700 nm	Reflectance	Classification SI and RI	Accuracy of 97.0% for Vis/NIR imaging and 100.0% for NIR imaging	Mo et al. [81]
Spinach leaves	Shelf life	400–1000 nm	Reflectance	Classification SAM, PLS-DA, and LEVE index	Over 95.0% of the leaves were classified into the same quality class by SAM and LEVE index	Diezma et al. [29]
	Shelf life and freshness (under plastic film)	400–1000 nm	Reflectance	PCA + ANOVA	Freshness characterization over time	Lara et al. [82]
	Shelf life and freshness	380–1030 nm, 874–1734 nm	Reflectance	PLS-DA, SVM, ELM	Accuracy > 92.0%	Zhu et al. [33]
	Escherichia coli	400–1000 nm	Reflectance	ANN	$R^2 = 0.97$	Siripatrawan et al. [58]
	Fecal contamination	456–950 nm 464–800 nm	Reflectance Fluorescence	PLS-DA	Fluorescence had the best results with accuracy from 87.0% to 100.0%	Everard et al. [30]
Rocket	Shelf life	400–1000 nm	Reflectance	PLSR	$R^2 = 0.73$–0.95	Chaudhry et al. [73]
	Vitamin C and phenols	400–1000 nm 900–1700 nm	Reflectance	PLSR	• Vitamin C: $R^2 = 0.76$ and RMSEP = 10.90 mg/100 g • Phenols: $R^2 = 0.78$ and RMSEP = 13.81 mg gallic acid/100 g	Chaudhry et al. [48]
Green amaranth leaves	Chlorophyll content	400–1000 nm	Reflectance	PLSR	$R^2 = 0.834$ RMSE = 0.067%	Mardhiyatna et al. [83]
Potato slices	Color and water content	400–1000 nm	Reflectance	PLS, SVM, and LS-SVM	LS-SVM had the best performances with R^2 above 0.80 for the prediction of both parameters	Xiao et al. [49]
	Starch content	380–1000 nm	Reflectance	PLSR	$R^2 = 0.95$ RMSEP = 1.63 g kg^{-1} RPD = 2.95	Wang et al. [52]
	Escherichia coli	400–1000 nm	Reflectance	PLSR, BP-NN	BP-NN model reached the best performances using both the full spectrum ($R^2 = 0.97$; RMSEP = 0.065 log CFU g^{-1}) and selected wavelengths ($R^2 = 0.88$; RMSEP = 0.142 log CFU g^{-1})	Li et al. [53]

Table 4. *Cont.*

Fresh-Cut Product	Quality Features	Spectral Range	Sensing Mode	Modeling Method	Performances	Reference
	Sulfur dioxide residue	975–1646 nm	Reflectance	SVM	Classification accuracy of 95.0%	Bai et al. [39]
Tomato	Color	325–985 nm	Reflectance	PLSR, PCR	For a*, hue, and L*, $R^2 > 0.86$; for b* and chroma, $R^2 = 0.4$–0.5	van Roy et al. [40]
	Cracking defects	1000–1700 nm	Reflectance	LDA	Accuracy of 91.7% (using full NIR spectrum) and of 80.6% (using only 4 wavelengths)	Lee et al. [35]
	Cracking defects	400–700 nm	Fluorescence	ANOVA + PCA	Accuracy >99.0%	Cho et al. [84]
	Firmness and sweetness	1000–1550 nm	Reflectance	PLSR	• Firmness: $R^2_p = 0.76$; SEP = 1.01 N • Sweetness: $R^2_p = 0.81$; SEP = 0.33	Rahman et al. [46]
	Firmness, color, pH, and SSC	400–1000 nm, 900–1700 nm	Reflectance	PLSR	Good performances in prediction were achieved: • SSC, firmness, and pH: $R^2_p > 0.85$; RPD > 3.0 • Color: RPD > 2.0	Ramos-Infante et al. [47]
Cucumber	Chilling injury	500–675 nm 675–1000 nm	Reflectance Transmittance	NB, SVM, KNN	SVM was the best, achieving an accuracy from 90.5% to 100%	Cen et al. [38]
Green bell pepper	Shelf life	464–799 nm	Fluorescence	LDA	LDA was successful in distinguishing the storage time at 0, 7, 14, and 21 days after cutting	Delwiche et al. [36]
	Chilling injury	400–1000 nm, 1000–2500 nm	Reflectance	PLS-DA	NER_{CV} = 83% with Vis-NIR model. NER_{CV} = 81% with NIR model	Babellahi et al. [34]
				PLSR	$R^2_{CV} = 0.79$, $RMSE_{CV} = 0.5$ days of storage at 4 °C	
Apple	SSC	400–1000 nm	Reflectance	PLSR	The best-performing models were • Case I: $R^2 = 0.802$ and RMSE = ±0.674°Brix • Case II: $R^2 = 0.871$ and RMSE = ±0.524°Brix • Case III: $R^2 = 0.876$ and RMSE = ±0.514°Brix	Mo et al. [44]
	DMC, TSC	1000–2500 nm	Reflectance	LOO-PLS	• Dry matter: $R^2_{CV} = 0.83$, $RMSE_{CV} = 9.7$ g kg^{-1}, RPD = 2.39 • TSC: $R^2_{CV} = 0.81$, $RMSE_{CV} = 8.4$ g kg^{-1}, RPD = 2.20	Lan et al. [54]

Table 4. *Cont.*

Fresh-Cut Product	Quality Features	Spectral Range	Sensing Mode	Modeling Method	Performances	Reference
	Browning–PPO activity	400–1000 nm	Reflectance	PLSR	An indirect detection of PPO activity was performed, and the results showed that the changes in the enzyme activity were mainly at wavelengths around 677 nm	Shrestha et al. [50]
Celery	Dietary fiber	378–1008 nm	Reflectance	PLS, Si-PLS, GA-Si-PLS	GA-Si-PLS had the best performances: • For IDF: $R^2_p = 0.96$; RMSEP = 1.18. • For SDF: $R^2_p = 0.97$; • RMSEP = 0.34	Yan et al. [42]
Fennel	SSC, phenol and antioxidant activity, sugars, and organic acids	400–1000 nm, 900–1700 nm	Reflectance	PLSR	• SSC: $R^2_p = 0.77$; RMSEP = 0.51°Brix; • Phenols: $R^2_p = 0.77$; RMSEP = 3.042 mg kg^{-1}	Amodio et al. [43]
				PLS-DA	NER$_P$ = 88.57%	
Bamboo shoots	Dietary fiber	400–1000 nm, 900–1700 nm	Reflectance	PLSR, PCR	SNV-PCA-PLSR achieved good prediction performances with $R^2_p = 0.902$ and RMSEP = 0.135	Xu et al. [41]
Onion, zucchini, garlic, and carrot	Foreign objects	420–730 nm	Fluorescence, Reflectance	Wavelength ratio classification method	Accuracy of 90.0–97.0% to detect different kinds of foreign materials	Cho [85]
Cabbage, carrot, green onion, onion, potato, radish, and zucchini	Foreign materials	400–1000 nm, 1000–2500 nm	Reflectance	PLS-DA	Accuracy of 99.0% with SWIR, 89.0% with Vis/NIR, and 64.0% with fluorescence	Tunny et al. [78]
		400–1000 nm	Fluorescence			

5. Conclusions and Perspectives

Since 2000, hyperspectral imaging technology has been demonstrating great potential in postharvest quality and safety assessment, introducing another element to bridge the gap between analysis in the lab and in the production process as a process analytical technology (PAT). This is playing a key role in the fourth industrial revolution where interest in the improvement of monitoring systems through the development of new interconnected sensors networks (IoT) is steadily growing. The fusion of different combinations of sensors leads to a multivariate statistical process control (MSPC) which provides (for each critical point) several highly correlated variables (optical and not) that can be handled by multivariate projection methods (e.g., PCA), enabling a reduction in data dimensionality by taking advantage of the correlated structure [86].

An optimized MSPC in fruit and vegetable fresh-cut production monitoring could solve the common shelf life problems of early decay, spoilage, etc., improving product standardization. Moreover, in some cases, the multivariate monitoring process could be extended from the maturation/growth process in the greenhouse to the various postharvest product processing steps, guaranteeing a complete supply-chain quality control.

However, the HSI devices currently on the market are laboratory instruments and portable devices where the cost remains a limit for the real application of these tools [87]. The cost limitations are not strictly related to the device itself but to the specific application. Indeed, even though the hyperspectral imaging technique can collect a large amount of

data, the application of only one device (in some cases) is not enough to cover all the critical points (after each processing step), the whole sample surface (big samples and/or stacked products), and detect foreign substances covered by the mass of a product (as in leafy fresh-cut samples, Section 4.1). In these circumstances, considering the application of several hyperspectral devices, the costs become prohibitive for most companies.

Currently, cost reduction is challenging and one of the main topics in HSI research studies. The first solution has been to build low-cost multispectral systems based on selected wavelengths identified by preliminary studies. Such an approach, although effective, extremely reduces the versatility of the instrument (which needs a recustomization if applied on different products and/or parameters) and the capability to refine the model. For these reasons, further studies have to continue in order to develop compact and cost-effective HSI devices to exponentially increase the versatility of applications.

In the last ten years, thanks to technological advancement and the development of silicon detectors used for the mass production of photographic instruments (i.e., commercial cameras and smartphones), researchers started to develop snapshot-based systems since they own a high optical throughput associated with an absence of artefacts due to scanning motion and an increased compactness due to no moving components. Since the optical range covered by silicon detectors (about 400–1000 nm) is the most used in the literature (Table 4) for fresh-cut production purposes, this technique offers a very promising solution to pre- and postharvest real-time imaging. However, the lower spatial and spectral resolution provided is still a key element to be studied.

One of the first works was proposed by Habel et al. (2012). The authors proposed a low-cost and compact spectral imaging Vis/NIR camera (design based on an unmodified consumer camera, Figure 13) with a mid-resolution hyperspectral mode that allows the spectral measurement of a whole image, with up to 5 nm spectral resolution and 120×120 spatial resolution. This "snapshot" system is based on the principles used in computed tomography. Computed tomography imaging spectrometers (CTISs) use a transmissive diffraction grating to split the incoming light into a number of spectral projections onto a single image plane. Then, spectra are recovered by solving an underdetermined linear system [88].
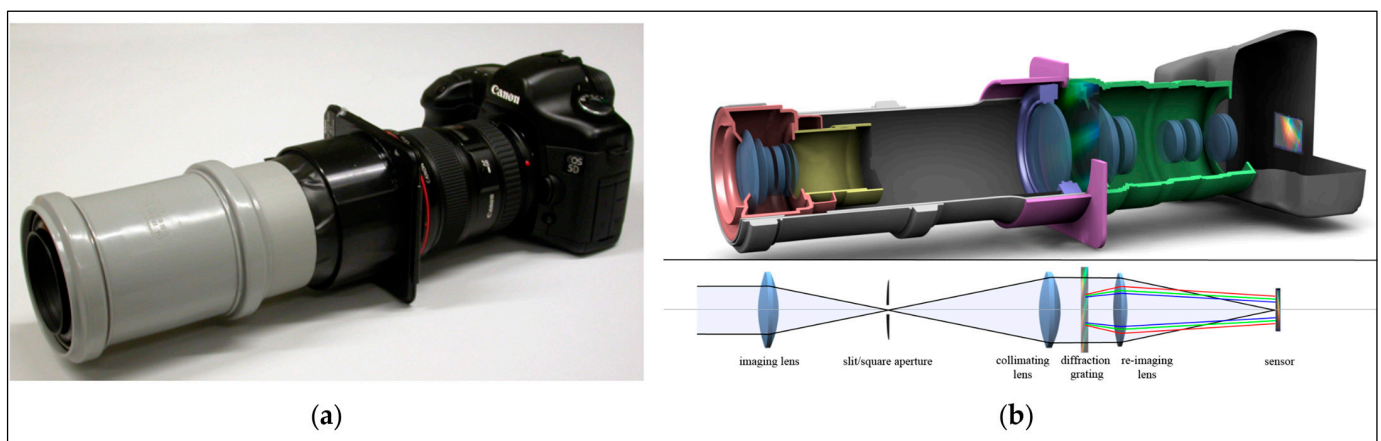

Figure 13. HSI device proposed by Habel et al. (2012): (**a**) assembled CTIS camera objective; (**b**) prototype camera objective (**top**) and principal optical path (**bottom**). Reprinted with permission from Ref. [88]. 2012, Elsevier.

On the same wave, Salazar-Vazquez and Mendez-Vazquez in 2020 took advantage of modern small-size high-resolution cameras (Raspberry PI NoIR camera), electronics, and optics to develop a robust low-cost HSI device (Figure 14), which weighs up to 300 g, detects wavelengths from 400 nm–1052 nm, and generates up to 315 different wavebands with a spectral resolution up to 2 nm and a spatial resolution of 116×110 pixels.
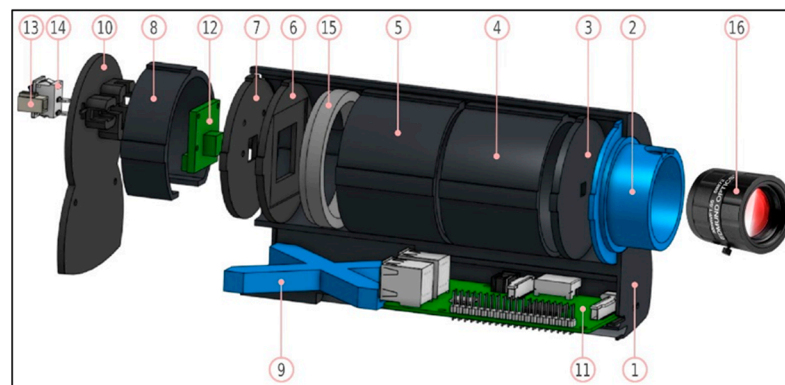
Figure 14. HSI device proposed by Salazar-Vazquez and Mendez-Vazquez (2020): (1) Case; (2) Front lens holder; (3) Square aperture; (4) Spacer 1; (5) Spacer 2; (6) Transmissive diffraction grating; (7) Camera holder; (8) Spacer 3; (9) Extension; (10) Lid; (11) Raspberry Pi 3 B+; (12) Raspberry Pi NoIR V2 Camera 8 Megapixels; (13) Power Supply Connector; (14) Power On/Off Switch; (15) +10 Macro 52 mm Lens; (16) Lens 35 mm C Series. Edmund Optics, model 59872. Reprinted with permission from Ref. [89]. 2020, Elsevier.

Although the authors proposed a very interesting plug-and-play HSI solution combined with a user-friendly GUI, the system shows a low-spectral outcome in the SWNIR region (750–1000 nm), suggesting a reduced analytical capability in food quality inspection. The use of this type of transmissive holographic double-axis diffraction grating (Figure 14) guarantees a significant cost reduction with a consistent loss of information in the SWNIR region.

However, such devices could be used to develop new applicative solutions using a fleet of distributed HSI sensors able to collect hyperspectral information from different checking spots [89].

Finally, recent advances in smartphone technologies have opened the door to the development of accessible highly portable HSI systems (Figure 15) capable of accurate, laboratory- and field-based hyperspectral data collection, providing a solid foundation for future developments of customized HSI tools for practical applications (i.e., quality inspection by operators in real-time) [90].

In this case, the authors adopted a linear transmissive diffraction grating which requires a movement system to analyze the entire sample and build the hypercube. Also, in this case, the spectral device is capable of covering the visible range (400–700 nm). Although the used diffraction grating has an efficiency of 20% in the SWNIR region, coupling this component with commercial smartphone cameras reduces the detectable optical range due to the presence of IR filters (used to reduce optical noise due to infrared radiation and improve image quality) commonly mounted in front of the camera detector.

However, the possibility to develop cost-effective systems able to cover a wider spectral range (from 400 to 1000) is ongoing, even though the performance of these tools still needs to be carefully evaluated (both in controlled and operative conditions) to demonstrate real applicability within the complex production realities from pre- to postharvest. Indeed, the capability to retrieve visible information (from 400 to 750) is an interesting starting point to solve different issues (raised in Table 4) like color–browning, chilling injuries, shelf life, and chlorophyll content.
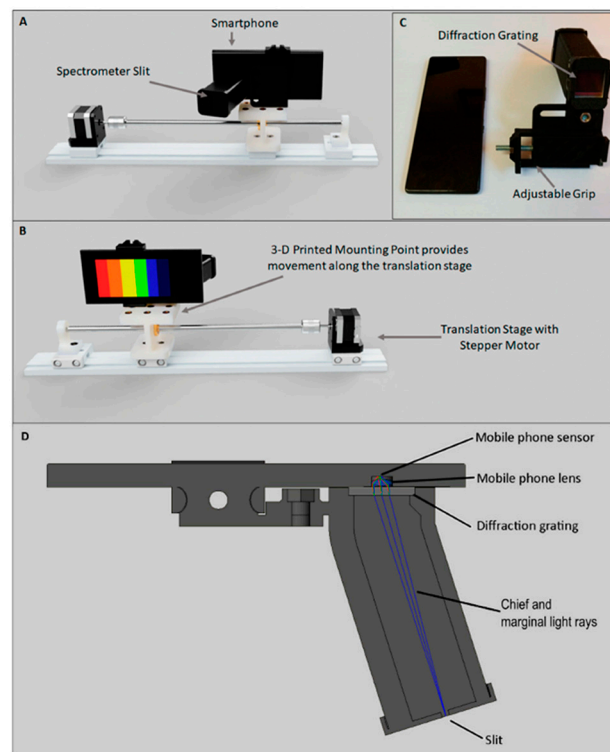
Figure 15. Schematic diagram proposed by Stuart et al. (2021) of a hyperspectral smartphone mounted to the translation stage: (**A**,**B**) show the front and rear views, respectively; (**C**) shows the hyperspectral smartphone attachment prior to connection with a smartphone, highlighting the location of the spectral optics; (**D**) shows a cross section of the smartphone spectrometer system and how the marginal and chief rays travel through the system. Reprinted with permission from Ref. [90]. 2021, Elsevier.

The arrival of this instrumentation in the scientific literature is the basis for the development of further real-time monitoring applications that allow the final introduction of this technology within the Industry 4.0 concept. The development of new, simple, and interconnected optical HSI systems (coupled with fast computing technologies based on parallel computing) would allow for the creation of the remote storage of optical databases, allowing for the continuous updating and refinement of the prediction performance of predictive models with the aim of continuously upgrading the control services at different and crucial steps from pre- to postharvest.

Institutional Review Board Statement: Not applicable.

Informed Consent Statement: Not applicable.

Data Availability Statement: Not applicable.

Conflicts of Interest: The authors declare no conflict of interest.

Abbreviations

ANN	Artificial Neural Network	NIR	Near-infrared
ANOVA	Analysis of Variance	PAT	Process Analytical Technology
AOTF	Acousto-Optic Tunable Filter	PC	Principal Component
CCD	Charge-Coupled Device	PCA	Principal Component Analysis
CFU	Colony-Forming Unit	PCR	Principal Component Regression
CMOS	Complementary Metal-Oxide-Semiconductor	PLS-DA	Partial Least Square–Discriminant Analysis
CTIS	Computed Tomography Imaging Spectrometer	PLSR	Partial Least Square Regression
DMC	Dry Matter Content	PPO	Polyphenol-Oxidase
ELM	Extreme Learning Machine	R2	Coefficient of Determination
ETFs	Electronically Tunable Filters	R2CV	Coefficient of Determination in Cross-Validation
FMs	Foreign materials	R2p	Coefficient of Determination in Prediction
GA-Si-PLS	Genetic Synergy Interval Partial Least Square	RI	Ratio Imaging
Ge	Germanium	RMSE	Root Mean Square Error
HSI	Hyperspectral Imaging or Hyperspectral Image	RMSECV	Root Mean Square Error in Cross-Validation
IDF	Insoluble Dietary Fiber	RMSEP	Root Mean Square Error in prediction
InGaAs	Indium Gallium Arsenide	ROI	Region of Interest
InSb	Indium Antimonite	SAM	Spectral Angle Mapper
IoT	Internet of Things	SDF	Soluble Dietary Fibre
KNN	K-Nearest Neighbor	SG	Savitzky–Golay
LCTF	Liquid Crystal Tunable Filter	SI	Subtraction Imaging
LDA	Linear Discriminant Analysis	Si	Silicon
LEDI	Lettuce Decay Index	SIMCA	Soft Independent Modeling by Class Analogy
LEDs	Light-Emitting Diodes	Si-PLS	Synergy Interval–Partial Least Square
LEVE	Leafy Vegetable Evolution	SNV	Standard Normal Variate
LOO-PLS	Leave-One-Out Partial Least Square	SPAD	Soil Plant Analysis Development
LS-SVM	Least Square Support Vector Machine	SSC	Soluble Solid Content
MAP	Modified Atmosphere Packaging	SVM	Support Vector Machine
MLR	Multiple Linear Regression	SVR	Support Vector Machine Regression
MSC	Multiplicative Scatter Correction	SWIR	Shortwave Infrared
MSPC	Multivariate Statistical Process Control	TSC	Total Sugar Content
MTC or HgCdTe	Mercury Cadmium Tellurium	UV	Ultraviolet
MVE	Minimum Volume Ellipsoid	VIP	Variable Importance in Projection
NB	Naïve Bayes	Vis	Visible
NER	Non Error Rate		

References

1. Colelli, G.; Elia, A. Physiological and technological aspects of fresh-cut horticultural products. *Italus Hortus* **2009**, *16*, 55–78.
2. Lu, Y.; Saeys, W.; Kim, M.; Peng, Y.; Lu, R. Hyperspectral imaging technology for quality and safety evaluation of horticultural products: A review and celebration of the past 20-year progress. *Postharvest Biol. Technol.* **2020**, *170*, 111318. [CrossRef]
3. Lu, Y.; Huang, Y.; Lu, R. Innovative hyperspectral imaging-based techniques for quality evaluation of fruits and vegetables: A review. *Appl. Sci.* **2017**, *7*, 189. [CrossRef]
4. Wu, D.; Sun, D.W. Advanced applications of hyperspectral imaging technology for food quality and safety analysis and assessment: A review—Part I: Fundamentals. *Innov. Food Sci. Emerg. Technol.* **2013**, *19*, 1–14. [CrossRef]
5. Siche, R.; Vejarano, R.; Aredo, V.; Velasquez, L.; Saldana, E.; Quevedo, R. Evaluation of food quality and safety with hyperspectral imaging (HSI). *Food Eng. Rev.* **2016**, *8*, 306–322. [CrossRef]
6. Lu, B.; Dao, P.D.; Liu, J.; He, Y.; Shang, J. Recent advances of hyperspectral imaging technology and applications in agriculture. *Remote Sens.* **2020**, *12*, 2659. [CrossRef]
7. Gowen, A.A.; O'Donnell, C.P.; Cullen, P.J.; Downey, G.; Frias, J.M. Hyperspectral imaging–an emerging process analytical tool for food quality and safety control. *Trends Food Sci. Technol.* **2007**, *18*, 590–598. [CrossRef]
8. Martinsen, P.; Schaare, P. Measuring soluble solids distribution in kiwifruit using near-infrared imaging spectroscopy. *Postharvest Biol. Technol.* **1998**, *14*, 271–281. [CrossRef]

9.   Nicolai, B.M.; Beullens, K.; Bobelyn, E.; Peirs, A.; Saeys, W.; Theron, K.I.; Lammertyn, J. Nondestructive measurement of fruit and vegetable quality by means of NIR spectroscopy: A review. *Postharvest Biol. Technol.* **2007**, *46*, 99–118. [CrossRef]

10.   Amigo, J.M.; Grassi, S. Configuration of hyperspectral and multispectral imaging systems. In *Data Handling in Science and Technology*; Elsevier: Amsterdam, The Netherlands, 2019; Volume 32, pp. 17–34.

11.   Lodhi, V.; Chakravarty, D.; Mitra, P. Hyperspectral imaging system: Development aspects and recent trends. *Sens. Imaging* **2019**, *20*, 35. [CrossRef]

12.   Qin, J. Hyperspectral imaging instruments. In *Hyperspectral Imaging for Food Quality Analysis and Control*; Academic Press: Cambridge, MA, USA, 2010; pp. 129–172.

13.   Marini, F.; Amigo, J.M. Unsupervised exploration of hyperspectral and multispectral images. In *Data Handling in Science and Technology*; Elsevier: Amsterdam, The Netherlands, 2019; Volume 32, pp. 93–114.

14.   Mobaraki, N.; Amigo, J.M. HYPER-Tools. A graphical user-friendly interface for hyperspectral image analysis. *Chemom. Intell. Lab. Syst.* **2018**, *172*, 174–187. [CrossRef]

15.   Laura, J.R.; Gaddis, L.R.; Anderson, R.B.; Aneece, I.P. Introduction to the Python Hyperspectral Analysis Tool (PyHAT). In *Machine Learning for Planetary Science*; Elsevier: Amsterdam, The Netherlands, 2022; pp. 55–90.

16.   Jiang, H.; Yoon, S.C.; Zhuang, H.; Wang, W.; Li, Y.; Lu, C.; Li, N. Non-destructive assessment of final color and pH attributes of broiler breast fillets using visible and near-infrared hyperspectral imaging: A preliminary study. *Infrared Phys. Technol.* **2018**, *92*, 309–317. [CrossRef]

17.   Amigo, J.M.; Santos, C. Preprocessing of hyperspectral and multispectral images. In *Data Handling in Science and Technology*; Elsevier: Amsterdam, The Netherlands, 2019; Volume 32, pp. 37–53.

18.   Biancolillo, A.; Marini, F. Chemometrics applied to plant spectral analysis. In *Comprehensive Analytical Chemistry*; Elsevier: Amsterdam, The Netherlands, 2018; Volume 80, pp. 69–104.

19.   Boulet, J.C.; Roger, J.M. Pretreatments by means of orthogonal projections. *Chemom. Intell. Lab. Syst.* **2012**, *117*, 61–69. [CrossRef]

20.   Oliveri, P.; Malegori, C.; Simonetti, R.; Casale, M. The impact of signal pre-processing on the final interpretation of analytical outcomes–A tutorial. *Anal. Chim. Acta* **2019**, *1058*, 9–17. [CrossRef]

21.   Rinnan, Å. Pre-processing in vibrational spectroscopy–when, why and how. *Anal. Methods* **2014**, *6*, 7124–7129. [CrossRef]

22.   Biancolillo, A.; Marini, F.; Ruckebusch, C.; Vitale, R. Chemometric strategies for spectroscopy-based food authentication. *Appl. Sci.* **2020**, *10*, 6544. [CrossRef]

23.   Maimon, O.; Rokach, L. Introduction to supervised methods. In *Data Mining and Knowledge Discovery Handbook*; Springer: Boston, MA, USA, 2005; pp. 149–164.

24.   Nasteski, V. An overview of the supervised machine learning methods. *Horizons. b* **2017**, *4*, 51–62. [CrossRef]

25.   de la Ossa, M.Á.F.; Amigo, J.M.; García-Ruiz, C. Detection of residues from explosive manipulation by near infrared hyperspectral imaging: A promising forensic tool. *Forensic Sci. Int.* **2014**, *242*, 228–235. [CrossRef] [PubMed]

26.   Torres, I.; Amigo, J.M. An overview of regression methods in hyperspectral and multispectral imaging. *Data Handl. Sci. Technol.* **2019**, *32*, 205–230.

27.   Amigo, J.M.; Martí, I.; Gowen, A. Hyperspectral imaging and chemometrics: A perfect combination for the analysis of food structure, composition and quality. In *Data Handling in Science and Technology*; Elsevier: Amsterdam, The Netherlands, 2013; Volume 28, pp. 343–370.

28.   Liakos, K.G.; Busato, P.; Moshou, D.; Pearson, S.; Bochtis, D. Machine learning in agriculture: A review. *Sensors* **2018**, *18*, 2674. [CrossRef]

29.   Diezma, B.; Lleó, L.; Roger, J.M.; Herrero-Langreo, A.; Lunadei, L.; Ruiz-Altisent, M. Examination of the quality of spinach leaves using hyperspectral imaging. *Postharvest Biol. Technol.* **2013**, *85*, 8–17. [CrossRef]

30.   Everard, C.D.; Kim, M.S.; Lee, H. A comparison of hyperspectral reflectance and fluorescence imaging techniques for detection of contaminants on spinach leaves. *J. Food Eng.* **2014**, *143*, 139–145. [CrossRef]

31.   Rady, A.; Guyer, D.; Lu, R. Evaluation of sugar content of potatoes using hyperspectral imaging. *Food Bioprocess Technol.* **2015**, *8*, 995–1010. [CrossRef]

32.   Pu, Y.Y.; Sun, D.W.; Buccheri, M.; Grassi, M.; Cattaneo, T.M.; Gowen, A. Ripeness classification of bananito fruit (Musa acuminata, AA): A comparison study of visible spectroscopy and hyperspectral imaging. *Food Anal. Methods* **2019**, *12*, 1693–1704. [CrossRef]

33.   Zhu, S.; Feng, L.; Zhang, C.; Bao, Y.; He, Y. Identifying freshness of spinach leaves stored at different temperatures using hyperspectral imaging. *Foods* **2019**, *8*, 356. [CrossRef]

34.   Babellahi, F.; Paliwal, J.; Erkinbaev, C.; Amodio, M.L.; Chaudhry, M.M.A.; Colelli, G. Early detection of chilling injury in green bell peppers by hyperspectral imaging and chemometrics. *Postharvest Biol. Technol.* **2020**, *162*, 111100. [CrossRef]

35.   Lee, H.; Kim, M.S.; Jeong, D.; Chao, K.; Cho, B.K.; Delwiche, S.R. Hyperspectral near-infrared reflectance imaging for detection of defect tomatoes. In *Sensing for Agriculture and Food Quality and Safety Iii*; SPIE: Bellingham, WA, USA, 2011; Volume 8027, pp. 148–156.

36.   Delwiche, S.R.; Stommel, J.R.; Kim, M.S.; Vinyard, B.T.; Esquerre, C. Hyperspectral fluorescence imaging for shelf life evaluation of fresh-cut Bell and Jalapeno Pepper. *Sci. Hortic.* **2019**, *246*, 749–758. [CrossRef]

37.   Ríos-Reina, R.; Callejón, R.M.; Amigo, J.M. Feasibility of a rapid and non-destructive methodology for the study and discrimination of pine nuts using near-infrared hyperspectral analysis and chemometrics. *Food Control.* **2021**, *130*, 108365. [CrossRef]

38.	Cen, H.; Lu, R.; Zhu, Q.; Mendoza, F. Nondestructive detection of chilling injury in cucumber fruit using hyperspectral imaging with feature selection and supervised classification. *Postharvest Biol. Technol.* **2016**, *111*, 352–361. [CrossRef]

39.	Bai, X.; Xiao, Q.; Zhou, L.; Tang, Y.; He, Y. Detection of sulfite dioxide residue on the surface of fresh-cut potato slices using near-infrared hyperspectral imaging system and portable near-infrared spectrometer. *Molecules* **2020**, *25*, 1651. [CrossRef]

40.	van Roy, J.; Keresztes, J.C.; Wouters, N.; De Ketelaere, B.; Saeys, W. Measuring colour of vine tomatoes using hyperspectral imaging. *Postharvest Biol. Technol.* **2017**, *129*, 79–89. [CrossRef]

41.	Xu, X.Y.; Xie, W.G.; Xiang, C.; You, Q.; Tian, X.G. Predicting the dietary fiber content of fresh-cut bamboo shoots using a visible and near-infrared hyperspectral technique. *J. Food Meas. Charact.* **2023**, *17*, 3218–3227. [CrossRef]

42.	Yan, L.; Xiong, C.; Qu, H.; Liu, C.; Chen, W.; Zheng, L. Non-destructive determination and visualisation of insoluble and soluble dietary fibre contents in fresh-cut celeries during storage periods using hyperspectral imaging technique. *Food Chem.* **2017**, *228*, 249–256. [CrossRef]

43.	Amodio, M.L.; Capotorto, I.; Chaudhry, M.M.A.; Colelli, G. The use of hyperspectral imaging to predict the distribution of internal constituents and to classify edible fennel heads based on the harvest time. *Comput. Electron. Agric.* **2017**, *134*, 1–10. [CrossRef]

44.	Mo, C.; Kim, M.S.; Kim, G.; Lim, J.; Delwiche, S.R.; Chao, K.; Lee, H.; Cho, B.K. Spatial assessment of soluble solid contents on apple slices using hyperspectral imaging. *Biosyst. Eng.* **2017**, *159*, 10–21. [CrossRef]

45.	Zhu, H.; Chu, B.; Fan, Y.; Tao, X.; Yin, W.; He, Y. Hyperspectral imaging for predicting the internal quality of kiwifruits based on variable selection algorithms and chemometric models. *Sci. Rep.* **2017**, *7*, 1–13. [CrossRef]

46.	Rahman, A.; Park, E.; Bae, H.; Cho, B.K. Hyperspectral imaging technique to evaluate the firmness and the sweetness index of tomatoes. *Korean J. Agric. Sci.* **2018**, *45*, 823–837.

47.	Ramos-Infante, S.J.; Suárez-Rubio, V.; Luri-Esplandiu, P.; Sáiz-Abajo, M.J. Assessment Of Tomato Quality Characteristics Using Vis/Nir Hyperspectral Imaging and Chemometrics. In Proceedings of the 2019 10th Workshop on Hyperspectral Imaging and Signal Processing: Evolution in Remote Sensing (WHISPERS), Amsterdam, The Netherlands, 24–26 September 2019; IEEE: Piscataway, NJ, USA; pp. 1–5.

48.	Chaudhry, M.M.; Amodio, M.L.; Amigo, J.M.; de Chiara, M.L.; Babellahi, F.; Colelli, G. Feasibility study for the surface prediction and mapping of phytonutrients in minimally processed rocket leaves (Diplotaxis tenuifolia) during storage by hyperspectral imaging. *Comput. Electron. Agric.* **2020**, *175*, 105575. [CrossRef]

49.	Xiao, Q.; Bai, X.; He, Y. Rapid screen of the color and water content of fresh-cut potato tuber slices using hyperspectral imaging coupled with multivariate analysis. *Foods* **2020**, *9*, 94. [CrossRef]

50.	Shrestha, L.; Kulig, B.; Moscetti, R.; Massantini, R.; Pawelzik, E.; Hensel, O.; Sturm, B. Comparison between hyperspectral imaging and chemical analysis of polyphenol oxidase activity on fresh-cut apple slices. *J. Spectrosc.* **2020**, *2020*, 7012525. [CrossRef]

51.	Eshkabilov, S.; Lee, A.; Sun, X.; Lee, C.W.; Simsek, H. Hyperspectral imaging techniques for rapid detection of nutrient content of hydroponically grown lettuce cultivars. *Comput. Electron. Agric.* **2021**, *181*, 105968. [CrossRef]

52.	Wang, F.; Wang, C.; Song, S. A study of starch content detection and the visualization of fresh-cut potato based on hyperspectral imaging. *RSC Adv.* **2021**, *11*, 13636–13643. [CrossRef] [PubMed]

53.	Li, D.; Zhang, F.; Yu, J.; Chen, X.; Liu, B.; Meng, X. A rapid and non-destructive detection of *Escherichia coli* on the surface of fresh-cut potato slices and application using hyperspectral imaging. *Postharvest Biol. Technol.* **2021**, *171*, 111352. [CrossRef]

54.	Lan, W.; Jaillais, B.; Renard, C.M.; Leca, A.; Chen, S.; Le Bourvellec, C.; Bureau, S. A method using near infrared hyperspectral imaging to highlight the internal quality of apple fruit slices. *Postharvest Biol. Technol.* **2021**, *175*, 111497. [CrossRef]

55.	Lu, R.; Peng, Y. Hyperspectral scattering for assessing peach fruit firmness. *Biosyst. Eng.* **2006**, *93*, 161–171. [CrossRef]

56.	Peng, Y.; Lu, R. Analysis of spatially resolved hyperspectral scattering images for assessing apple fruit firmness and soluble solids content. *Postharvest Biol. Technol.* **2008**, *48*, 52–62. [CrossRef]

57.	Rajkumar, P.; Wang, N.; EImasry, G.; Raghavan, G.S.V.; Gariepy, Y. Studies on banana fruit quality and maturity stages using hyperspectral imaging. *J. Food Eng.* **2012**, *108*, 194–200. [CrossRef]

58.	Siripatrawan, U.; Makino, Y.; Kawagoe, Y.; Oshita, S. Rapid detection of *Escherichia coli* contamination in packaged fresh spinach using hyperspectral imaging. *Talanta* **2011**, *85*, 276–281. [CrossRef] [PubMed]

59.	Zhang, H.; Paliwal, J.; Jayas, D.S.; White, N.D.G. Classification of fungal infected wheat kernels using near-infrared reflectance hyperspectral imaging and support vector machine. *Trans. ASABE* **2007**, *50*, 1779–1785. [CrossRef]

60.	Chen, S.; Zhang, F.; Ning, J.; Liu, X.; Zhang, Z.; Yang, S. Predicting the anthocyanin content of wine grapes by NIR hyperspectral imaging. *Food Chem.* **2015**, *172*, 788–793. [CrossRef]

61.	Pang, T.; Rao, L.; Chen, X.; Cheng, J. Impruved prediction of soluble solid content of apple using a combination of spectral and textural features of hyperspectral images. *J. Appl. Spectrosc.* **2021**, *87*, 1196–1205. [CrossRef]

62.	Francis, G.A.; Gallone, A.; Nychas, G.J.; Sofos, J.N.; Colelli, G.; Amodio, M.L.; Spano, G. Factors affecting quality and safety of fresh-cut produce. *Crit. Rev. Food Sci. Nutr.* **2012**, *52*, 595–610. [CrossRef] [PubMed]

63.	Lorente, D.; Aleixos, N.; Gómez-Sanchis, J.U.A.N.; Cubero, S.; García-Navarrete, O.L.; Blasco, J. Recent advances and applications of hyperspectral imaging for fruit and vegetable quality assessment. *Food Bioprocess Technol.* **2012**, *5*, 1121–1142. [CrossRef]

64. Özdoğan, G.; Lin, X.; Sun, D.W. Rapid and noninvasive sensory analyses of food products by hyperspectral imaging: Recent application developments. *Trends Food Sci. Technol.* **2021**, *111*, 151–165. [CrossRef]

65. Bhargava, A.; Bansal, A. Fruits and vegetables quality evaluation using computer vision: A review. *J. King Saud Univ.-Comput. Inf. Sci.* **2021**, *33*, 243–257. [CrossRef]

66. Pham, Q.T.; Liou, N.S. Hyperspectral Imaging System with Rotation Platform for Investigation of Jujube Skin Defects. *Appl. Sci.* **2020**, *10*, 2851. [CrossRef]

67. Artés–Hernández, F.; Gómez, P.; Artés–Carlero, F. Fisiologia postraccolta e tecnologia degli ortaggi di IV gamma. In *Valutazione della qualità di ortaggi di IV gamma*; Ferrante, A., Cattaneo, T., Eds.; ARACNE: Roma, Italy, 2010; pp. 19–46. ISBN 9788854829305.

68. Gaglio, R.; Craparo, V.; Francesca, N.; Settanni, L. Aspetti igienico-sanitari dei prodotti vegetali di IV gamma. *La Riv. Di Sci. Dell'Alimentazione* **2017**, *46*, 23–34.

69. Mo, C.; Kim, G.; Lim, J.; Kim, M.S.; Cho, H.; Cho, B.K. Detection of lettuce discoloration using hyperspectral reflectance imaging. *Sensors* **2015**, *15*, 29511–29534. [CrossRef]

70. Mo, C.; Kim, G.; Kim, M.S.; Lim, J.; Lee, K.; Lee, W.H.; Cho, B.K. On-line fresh-cut lettuce quality measurement system using hyperspectral imaging. *Biosyst. Eng.* **2017**, *156*, 38–50. [CrossRef]

71. Simko, I.; Jimenez-Berni, J.A.; Furbank, R.T. Detection of decay in fresh-cut lettuce using hyperspectral imaging and chlorophyll fluorescence imaging. *Postharvest Biol. Technol.* **2015**, *106*, 44–52. [CrossRef]

72. Cho, H.; Kim, M.S.; Kim, S.; Lee, H.; Oh, M.; Chung, S.H. Hyperspectral determination of fluorescence wavebands for multispectral imaging detection of multiple animal fecal species contaminations on romaine lettuce. *Food Bioprocess Technol.* **2018**, *11*, 774–784. [CrossRef]

73. Chaudhry, M.M.; Amodio, M.L.; Babellahi, F.; de Chiara, M.L.; Rubio, J.M.A.; Colelli, G. Hyperspectral imaging and multivariate accelerated shelf life testing (MASLT) approach for determining shelf life of rocket leaves. *J. Food Eng.* **2018**, *238*, 122–133. [CrossRef]

74. Tao, R.; Zhang, F.; Tang, Q.J.; Xu, C.S.; Ni, Z.J.; Meng, X.H. Effects of curcumin-based photodynamic treatment on the storage quality of fresh-cut apples. *Food Chem.* **2019**, *274*, 415–421. [CrossRef]

75. Ariana, D.P.; Lu, R. Quality evaluation of pickling cucumbers using hyperspectral reflectance transmittance imaging: Part, I. Development of a prototype. *Sens. Instrum. Food Qual. Saf.* **2008**, *2*, 144–151. [CrossRef]

76. Lu, R.; Ariana, D.P. Detection of fruit fly infestation in pickling cucumbers using a hyperspectral reflectance/transmittance imaging system. *Postharvest Biol. Technol.* **2013**, *81*, 44–50. [CrossRef]

77. Blasco, J.; Munera, S.; Cubero, S.; Aleixos, N. Food and feed production. In *Data Handling in Science and Technology*; Elsevier: Amsterdam, The Netherlands, 2019; Volume 32, pp. 475–491.

78. Tunny, S.S.; Kurniawan, H.; Amanah, H.Z.; Baek, I.; Kim, M.S.; Chan, D.; Faqeerzada, M.A.; Wakholi, C.; Cho, B.K. Hyperspectral imaging techniques for detection of foreign materials from fresh-cut vegetables. *Postharvest Biol. Technol.* **2023**, *201*, 112373. [CrossRef]

79. Mo, C.; Kim, G.; Lim, J. Online hyperspectral imaging system for evaluating quality of agricultural products. In *Optical Measurement Systems for Industrial Inspection X*; SPIE: Bellingham, WA, USA, 2017; Volume 10329, pp. 849–855.

80. Shurygin, B.; Chivkunova, O.; Solovchenko, O.; Solovchenko, A.; Dorokhov, A.; Smirnov, I.; Astashev, M.E.; Khort, D. Comparison of the Non-Invasive Monitoring of Fresh-Cut Lettuce Condition with Imaging Reflectance Hyperspectrometer and Imaging PAM-Fluorimeter. *Photonics* **2021**, *8*, 425. [CrossRef]

81. Mo, C.; Kim, G.; Kim, M.S.; Lim, J.; Lee, S.H.; Lee, H.S.; Cho, B.K. Discrimination methods for biological contaminants in fresh-cut lettuce based on VNIR and NIR hyperspectral imaging. *Infrared Phys. Technol.* **2017**, *85*, 1–12. [CrossRef]

82. Lara, M.A.; Lleó, L.; Diezma-Iglesias, B.; Roger, J.M.; Ruiz-Altisent, M. Monitoring spinach shelf-life with hyperspectral image through packaging films. *J. Food Eng.* **2013**, *119*, 353–361. [CrossRef]

83. Mardhiyatna Saputro, A.H.; Imawan, C. Chlorophylls content prediction of green amaranth (*Amaranthus tricolor* L.) leaves based on Vis-NIR image. In Proceedings of the 2017 International Conference on Electrical Engineering and Informatics (ICELTICs), Banda Aceh, Indonesia, 18–20 October 2017; IEEE: Piscataway, NJ, USA; pp. 235–238.

84. Cho, B.K.; Kim, M.S.; Baek, I.S.; Kim, D.Y.; Lee, W.H.; Kim, J.; Bae, H.; Kim, Y.S. Detection of cuticle defects on cherry tomatoes using hyperspectral fluorescence imagery. *Postharvest Biol. Technol.* **2013**, *76*, 40–49. [CrossRef]

85. Cho, B.K. Application of spectral imaging for safety inspection of fresh cut vegetables. *IOP Conf. Ser. Earth Environ. Sci.* **2021**, *686*, 012001. [CrossRef]

86. Kourti, T. The process analytical technology initiative and multivariate process analysis, monitoring and control. *Anal. Bioanal. Chem.* **2006**, *384*, 1043–1048. [CrossRef] [PubMed]

87. Pampuri, A.; Tugnolo, A.; Giovenzana, V.; Casson, A.; Pozzoli, C.; Brancadoro, L.; Guidetti, R.; Beghi, R. Application of a Cost-Effective Visible/Near Infrared Optical Prototype for the Measurement of Qualitative Parameters of Chardonnay Grapes. *Appl. Sci.* **2022**, *12*, 4853. [CrossRef]

88. Habel, R.; Kudenov, M.; Wimmer, M. Practical spectral photography. In *Computer Graphics Forum*; Blackwell Publishing Ltd.: Oxford, UK, 2012; Volume 31, pp. 449–458.

89. Salazar-Vazquez, J.; Mendez-Vazquez, A. A plug-and-play Hyperspectral Imaging Sensor using low-cost equipment. *HardwareX* **2020**, *7*, e00087. [CrossRef] [PubMed]

90. Stuart, M.B.; McGonigle, A.J.; Davies, M.; Hobbs, M.J.; Boone, N.A.; Stanger, L.R.; Zhu, C.; Pering, T.D.; Willmott, J.R. Low-cost hyperspectral imaging with a smartphone. *J. Imaging* **2021**, *7*, 136. [CrossRef]